Bohorquez P., Cañada-Pereira P., Jimenez-Ruiz P.J., del Moral-Erencia J.D. The fascination of a shallow-water theory for the formation of megaflood-scale dunes and antidunes. Earth-Science Reviews, 193: 91–108, 2019. T1 Q1 (2/200 Multidisciplinary Geoscience, IF 2019 = 9.7). https://doi.org/10.1016/j.earscirev.2019.03.021

The fascination of a shallow-water theory for the formation of megaflood-scale dunes and antidunes

P. Bohorquez[a,*], P. Cañada-Pereira[b], P.J. Jimenez-Ruiz[b], J.D. del Moral-Erencia[a]

[a] *Centro de Estudios Avanzados en Ciencias de la Tierra (CEACTierra), Universidad de Jaén. Campus de las Lagunillas, 23071 Jaén, Spain*

[b] *Área de Mecánica de Fluidos, Departamento de Ingeniería Mecánica y Minera, Universidad de Jaén. Campus de las Lagunillas, 23071 Jaén, Spain*

Abstract

Exceptional megaflood-scale bedforms on Earth are commonly associated with the catastrophic draining of glacial lakes in the late Pleistocene. The widest studied events have been the Missoula and Altai floods with 300-700 m flow depth, 1-20 m bedform height and 10-300 m wavelength. Nowadays, the Saint-Venant equations have succeeded at simulating the catastrophic glacial-lake drainage process numerically, but we still lack a depth-averaged morphodynamic theory able to predict the growth of dunes and antidunes. The disparity of spatial scales in megafloods prevents the use of non-depth-averaged rotational flow equations, motivating the present shallow-water theory for the formation of megaflood-scale bedforms.

We adopt a non-equilibrium sediment transport equation rooted in Einstein's pioneering work. Here we prove that the bed instability triggers to form dunes and antidunes simply by lagging the entrainment term for sediment mass conservation, or the bottom shear stress, with respect to the depth-averaged flow velocity. We formalise this result using a linear stability theory that captures the existence regions of dune and antidune in addition to the roll wave instability. Furthermore, in the spirit of Kennedy (*Annu. Rev. Fluid Mech.*, vol. 1, 1969, pp. 147–168), we derive a closed-form solution of growth rate and wave speed of the bedform. The nondimensional groups controlling the linear instabilities are the Froude number, $\mathcal{F}r$, the Shields parameter, Sh, and the grain roughness relative to flow depth, δ.

Subsequently, we simulate the drainage of the largest Missoula flood numerically to explain the formation of giant antidunes in the Camas Prairie (Montana, US) during the late stage of the megaflood. Also considered are large fields of gravel dunes in the Kuray-Chuja Lake Basin (Altai Mountains, Siberia). The simulated hydraulic conditions over bedforms in both basins yield values of the nondimensional parameters that lie in the theoretical region of dunes and antidunes according to the proposed theory and in situ measurements in sandy rivers and flume experiments.

Keywords: linear stability theory, sediment transport, Missoula and Altai Quaternary flood, dune, antidune

Contents

*Corresponding author.
Email address: patricio.bohorquez@ujaen.es (P. Bohorquez)

March 27, 2019

1. Introduction

Terrestrial megafloods were a global phenomenon with extraordinary spatial extent and repeated frequency, affecting the surface sedimentary geology across continents (for a review, see Baker, 2009, 2013). In the Central Asian mountain areas, a great megaflood from the Kuray-Chuja paleolake formed the largest fields of gravel dunes in the late Pleistocene (Baker et al., 1993; Carling, 1996, 1999; Rudoy, 2002; Herget, 2005), see Fig. 1a. They exhibit dimensions comparable to very large dunes in long sandy rivers (Bradley and Venditti, 2017) and the deep Yangtze River (Fig. 1b). In the famous glacial Lake Missoula, Pardee (1942) described giant dunes of coarse gravel and unusual trains of antidunes across the Camas Prairie (Montana, US), as shown in Fig. 1c, that resulted from the rapid drainage of the lake due to the sudden ice-dam failure in the Late Pleistocene (Baker, 1973, 2009). The paleohydraulic significance of the detailed stratification of such bedforms could be used to greatly improve the reconstruction of the flood events if the dynamical simulation of the flow field allowed the computation of the bedform evolution (Carling, 2013; Carling et al., 2016). Presently, lake draining models have been improved by incorporating the hydraulic interpretation of subaqueous bedforms (Bohorquez et al., 2016, 2019), but we still lack a shallow-water model allowing the direct numerical simulation of their formation.

The interest of a depth-averaged morphodynamic model capable of predicting the formation of large bedforms is broad. In cataclysmic flood studies, depth-averaged shallow-water equations have become the preferred flow model for the paleohydraulic reconstruction (Carling et al., 2010; Alho et al., 2010; Denlinger and O'Connell, 2010; Periáñez and Abril, 2015; Bohorquez et al., 2016; Winsemann et al., 2016; Abril-Hernández et al., 2018) since their introduction for lower-magnitude outburst floods (Carrivick, 2006; Bohorquez and Darby, 2008). The more involved depth-averaged morphodynamic model can evaluate the aggradation and degradation of the channel in flood events (Huang et al., 2014, 2015; Guan et al., 2015) and generic geophysical flows (García, 2007; Wu, 2007; Julien, 2010). Earlier attempts to predict the formation of dunes by means of the standard Saint-Venant-Exner equations concluded that the model at Froude numbers $\mathcal{F}r < 2$ unphysically damps one-dimensional bedforms (e.g., Reynolds, 1965; Gradowczyk, 1968; Balmforth and Provenzale, 2001), preventing the natural growth of dunes and, also, antidunes. The later use of a non-equilibrium transport theory succeeded at capturing upper-regime forms (Deigaard, 2006; Di Cristo et al., 2006; Vesipa et al., 2012; Bohorquez and Ancey, 2015; Greco et al., 2017). To the best of the authors' knowledge, the formulation of a morphodynamic shallow-water model that also predicts the large-scale subaqueous dunes remains an open problem.

Hence, we need to establish the basis of a unified morphodynamic formulation that permits the spontaneous growth of dunes in the subcritical regime and antidunes in supercritical flows, as it was done with potential (Kennedy, 1963, 1969) and rotational flow models (e.g. Dey, 2014, Ch. 8). Linear stability analysis is the required mathematical tool to achieve this goal (e.g. McLean,

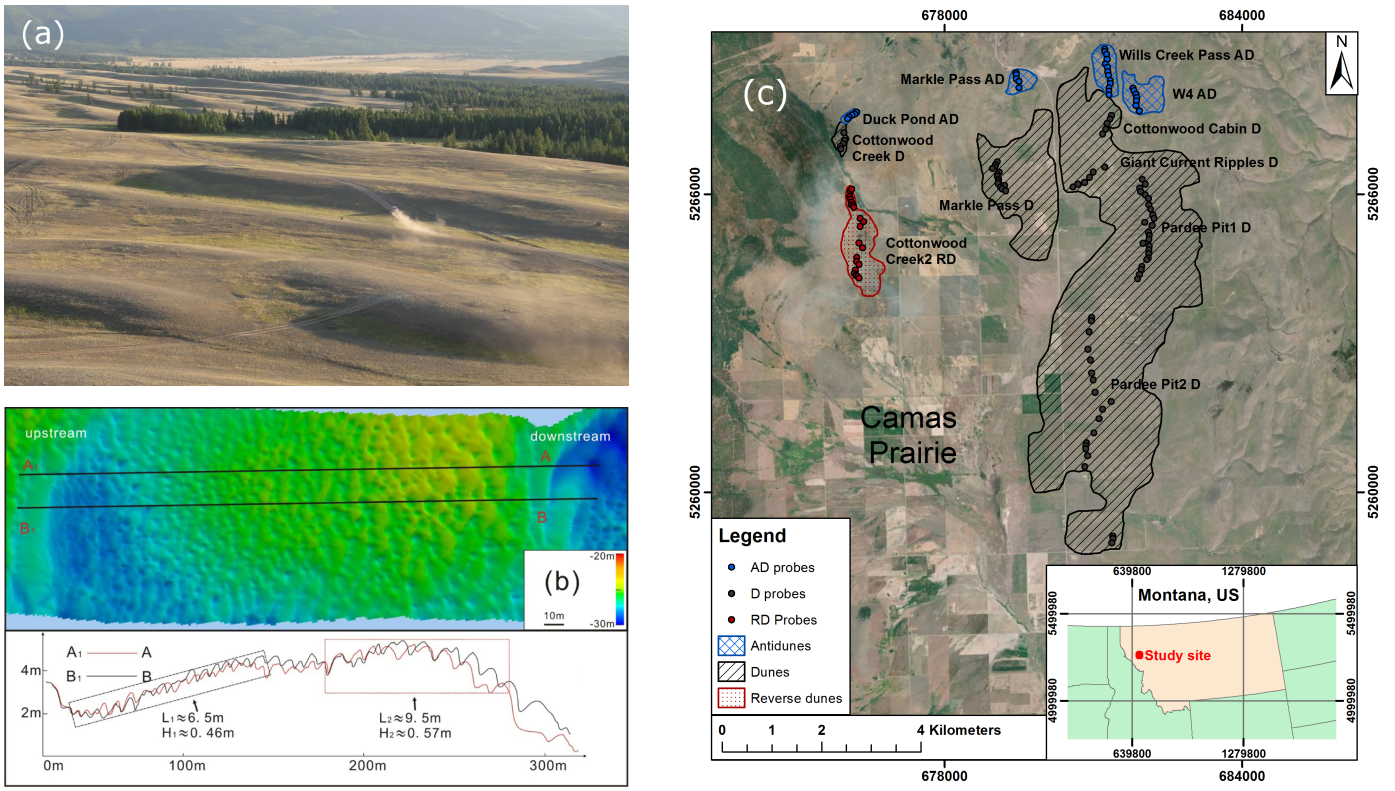

Fig. 1: (*a*) Field of giant gravel dunes in the Altai Mountains (Siberia). The car sets the scale. (*b*) Plan and long view of a very large dune in the Yangtze River (Chizhou, China), accompanied by secondary dunes (Shuwei et al., 2017). The average dimensions of the dune in a fluvial dominated regime are 204 m wavelength and 4 m height for a flow 10-30 m in depth at 0.78-0.99 m s^{-1}. (*c*) Location map of the Camas Prairie (Montana, US) showing the areas covered by giant dunes and antidunes visible in an aerial orthophoto.

1990). Dunes may form with a Froude number in the range of $\mathcal{F}r \lessapprox 0.7$, and the transition to antidune occurs for a higher value (Carling and Shvidchenko, 2002). Theory should account in addition for the relative depth with respect to the grain size as antidune have not been observed in deep rivers (Bradley and Venditti, 2017), and dunes do not develop in gravel-bed streams (Recking et al., 2009).

Here we show that the morphodynamical model by Bohorquez and Ancey (2015, 2016), which couples the Saint–Venant equation of hydraulic engineering to a bed-load model advocated by Ancey and Heyman (2014), can predict the dune/antidune instability of the erodible bed by lagging the entrainment term with respect to the depth-averaged flow velocity. Furthermore, the model deals with the roll wave instability of the free surface. Shallow-water equations make feasible the analytical treatment of the current linear stability theory, and allow us to capture the wavelength spectrum observed in flume experiments and river flows (Carling and Shvidchenko, 2002; Recking et al., 2009; Cheng, 2016; Bradley and Venditti, 2017).

The paper is organised as follows: the morphodynamic models relevant in paleohydrology are revisited in Section 2.1 (conservation laws of the water phase) and Section 2.2 (sediment continuity equation); their capability to capture the formation of bedforms is analysed in Section 2.3. Based on available experimental data at the laboratory and river (Section 3), we review the relevant nondimensional parameters that control the formation of dune/antidune, proposing a novel three-dimensional bedform diagram. Next, in Section 4, we proceed to prove the capability of the proposed morphodynamic model to predict the formation of such bedforms by using a linear stability analysis. Inspired in the

seminal work of Kennedy (1963, 1969), we also derive an analytical solution of the growth rate and wave speed of the bedform. The applicability of the bedform stability diagram to predict the developments of giant dunes and antidunes in a megaflood is subsequently shown in Section 5, where the case studies are the largest Missoula flood in Camas Prairie and the Altai megaflood in the Kuray-Chuja lakes. Conclusions are finally drawn in Section 6.

2. Morphodynamic models in paleohydrology

2.1. The Saint-Venant equations

Unsteady hydraulic modelling has become a standard in paleohydrology. Early illustrative examples of the potential of this technique include the reconstruction from high-magnitude (Carrivick, 2006) to small-magnitude outburst floods (Bohorquez and Darby, 2008). Later, the applicability to retrodict the dynamics of catastrophic late Pleistocene glacial-lake drainage was proved in notable case studies such as the largest Missoula draining (Alho et al., 2010; Denlinger and O'Connell, 2010), the Kuray-Chuja megaflood in the Altai Mountains (Carling et al., 2010; Bohorquez et al., 2016), along the margin of the Middle Pleistocene Scandinavian Ice Sheet (Winsemann et al., 2016) and the Lake Bonneville (Abril-Hernández et al., 2018). Morphological changes were neglected by assuming a fixed bed which approach is consistent with the lack of significant changes in basin capacity in the late Pleistocene (Bohorquez et al., 2016). The direct numerical simulation of the older, and even higher-magnitude, Zanclean flood offered the possibility to quantify marine mega-floods (Periáñez and Abril, 2015).

The shallow-water equations, better known as the Saint-Venant equations, were adopted in the studies cited above to describe the motion of the water phase. Independently of the number of spatial dimensions considered in the modelling (i.e. one- or two-dimensional flow), or the system of coordinate used to express the governing equations (Cartesian or curvilinear), the conservation laws of mass and momentum can be obtained by depth-averaging the Navier–Stokes equations for clear water and can be written in compact form as

$$\frac{\partial \widehat{\eta}}{\partial \widehat{t}} + \nabla \cdot (\widehat{\eta}\,\widehat{\boldsymbol{u}}) = 0\,, \tag{1}$$

$$\frac{\partial \widehat{\eta}\,\widehat{\boldsymbol{u}}}{\partial \widehat{t}} + \nabla \cdot (\widehat{\eta}\,\widehat{\boldsymbol{u}}\,\widehat{\boldsymbol{u}}) + \nabla\left(\frac{\widehat{g}\,\widehat{\eta}^2}{2}\right) = -\widehat{g}\,\widehat{\eta}\,\nabla\widehat{z} - \frac{\widehat{\boldsymbol{\tau}}_b^{\varphi}}{\widehat{\rho}} + \nabla \cdot (\widehat{\nu}\nabla\widehat{\boldsymbol{u}})\,, \tag{2}$$

where $\widehat{t}$ is the time, $\widehat{\eta}$ is the depth of the water measured along the vertical coordinate, $\widehat{\boldsymbol{u}}$ is the depth-averaged velocity vector, $\widehat{z}$ is the bed altitude and $\widehat{g}$ is the acceleration due to gravity. The source terms in the momentum equation are the bed slope $\nabla\widehat{z}$ and the bottom shear stress $\widehat{\boldsymbol{\tau}}_b/\widehat{\rho}$, in which $\widehat{\rho}$ is the water density. The extra term, $\nabla \cdot (\widehat{\nu}\nabla\widehat{\boldsymbol{u}})$, represents a depth-averaged Reynolds stress where $\widehat{\nu}$ is the eddy viscosity.

Both the dimensional-based Darcy-Weisbach friction factor, f, and Manning's roughness coefficient, $\widehat{n}$, can be used for evaluating the friction term in (2) by setting

$$\frac{\widehat{\boldsymbol{\tau}}_b^{\varphi}}{\widehat{\rho}} = \frac{f}{8}\widehat{\boldsymbol{u}}^{\varphi}|\widehat{\boldsymbol{u}}^{\varphi}| = \frac{\widehat{g}\,\widehat{n}^2}{\widehat{\eta}^{1/3}}\widehat{\boldsymbol{u}}^{\varphi}|\widehat{\boldsymbol{u}}^{\varphi}|\,. \tag{3}$$

Following Kennedy (1963), we propose the incorporation of a phase-lag between the bottom shear stress and the mean velocity in (3). Kennedy used a potential theory to describe the flow field in the outer region which occupies more than 80% of the flow depth for Reynolds numbers $\mathcal{R}e \sim O(\widehat{u}_0\,\widehat{\eta}_0\,\widehat{\rho}/\widehat{\mu}) > O(10^5)$, see Nezu and Nakagawa (1993), where $\widehat{\mu}$ is the dynamic viscosity of water, $\widehat{\eta}_0$ and $\widehat{u}_0 = |\widehat{\boldsymbol{u}}_0|$ are the characteristic value of the flow depth and velocity, respectively. The distribution of bottom shear stress was unresolved in his potential theory and, subsequently, he had to prescribe its phase lag. Similarly, the Saint-Venant equations require a closure law for the friction force. The inclusion of the lagged velocity in the friction term (3) serves the purpose of providing the effect caused by the out-of-phase shear stress proven in theoretical boundary-layer

theories, and verified by experimental measurements and numerical simulations (see, for a review, Charru et al., 2013).

We aim to provide a framework where the formation of dunes and antidunes can be studied within a shallow-water formulation. Since Kennedy, it is well-known that a lag between the shear rate and the flow velocity is required in order for the instability to take place. Subsequently, the lagged velocity is evaluated as $\widehat{\boldsymbol{u}}^{\varphi}(\widehat{\mathbf{x}},\widehat{t}) = \widehat{\boldsymbol{u}}(\widehat{\mathbf{x}} + \varphi\,\widehat{\mathbf{k}}/|\widehat{\mathbf{k}}|^2,\widehat{t})$. Substituting into (3) yields a friction law consistent with depth-averaged results from rotational flow models that determine theoretically the phase lag φ using a heavier formalism than the shallow-water equations (Fourrière et al., 2010; Andreotti et al., 2012). The simpler approach used in this work is empirical as we set $\varphi = 0$ and $\pi/2$ for the antidune (Heyman et al., 2016) and dune (Frederick and Hanratty, 1988), respectively. For the sake of the clarity, the superscript φ is used to identify the lagged terms in the current paper.

Simulated flooding areas, maps of water flow depth and velocity magnitude can thus be obtained by solving the shallow-water equations numerically. Early slope-conveyance, slope-area methods and step-backwater analysis became standards for paleohydraulic reconstruction in confined valleys (Feldman, 1981; Lumbroso and Gaume, 2012; Herget et al., 2014), where an increase in flood discharge results in a large increase in the stage (Baker, 1987). During the last decade, efficient open-source software packages for two-dimensional flow in complex floodplains, e.g. Dassflow-Shallow 2.0 (Monnier et al., 2016) and GeoClaw (Berger et al., 2011), has attracted growing attention due to recent advances in computational power and the availability of global Digital Elevation Models. The 2D version of the Saint-Venant equations captures backwater effects, hydraulic jumps, the backflood of tributary and wet/dry fronts (Wu, 2007). The thoughtful comparison of modelled hydraulic variables against inferred values from paleostage indicators and instrumental data supports the paleoflood reconstruction method over fixed beds (George, 2011; Bohorquez, 2016; Bohorquez and del Moral-Erencia, 2017).

In this work, the two-dimensional shallow-water equations were solved numerically using a second-order accurate HLLC approximate Riemann solver with MUSCL reconstruction, and an implicit-explicit Runge-Kutta (IMEX) time integration —denoted by IMEX-SSP(3,2,2)/MUSCL with MP limiter in Monnier et al. (2016).

2.2. Sediment transport formulations

Dynamical simulations of floods over a moveable bed at real scale are exceptional independently of the magnitude of the peak discharge (Huang et al., 2014, 2015; Guan et al., 2015). Such an involved technique proved valuable to quantify aggradation and degradation processes of the channel as well as the formation of lateral bars. The preferred formulation to dictate the temporal evolution of the bed was a non-equilibrium sediment transport model.

At the laboratory scale, the non-equilibrium model outperforms simpler approaches, as shown in numerous case studies (e.g. Cao et al., 2004; Wu, 2007; El Kadi Abderrezzak and Paquier, 2009; Cao et al., 2010; Zhang et al., 2013; Li and Qi, 2015; Bohorquez and Ancey, 2016; Cao et al., 2017; Wu et al., 2018). These examples provide evidence that a non-equilibrium sediment transport formulation performs better than the classic Exner equation. Some authors prefer to express the morphodynamic model in terms of an equivalent depth-averaged volumetric concentration of sediment, whereas others keep the mean particle activity as the unknown to be determined (Charru, 2006; Lajeunesse et al., 2010).

Without loss of generality, sediment transport is described using the following advection–diffusion equation (Bohorquez and Ancey, 2015):

$$\frac{\partial\widehat{\gamma}}{\partial\widehat{t}} + \nabla\cdot(\widehat{\boldsymbol{u}}_p\widehat{\gamma}) - \widehat{\alpha}\nabla^2\widehat{\gamma} = \widehat{\kappa}\,(\widehat{\gamma}^{\varphi}_{ss} - \widehat{\gamma})\ , \qquad (4)$$

where $\widehat{\gamma}$ is the mean particle activity (solid volume of particles in motion per unit streambed area), $\widehat{\boldsymbol{u}}_p$ is the mean velocity of moving particles, and $\widehat{\alpha}$ is the particle diffusivity. In the classic approach, hereafter referred to as equilibrium transport theory, the mean particle activity is defined

as $\widehat{\gamma} = \widehat{\gamma}_{ss}$, in which $\widehat{\gamma}_{ss}$ depends on the Shields number

$$Sh = \frac{|\widehat{\boldsymbol{\tau}}_b|}{\widehat{\rho}\,(s-1)\,\widehat{g}\,\widehat{d}}, \tag{5}$$

$\widehat{d}$ is the mean particle diameter and the constant parameter s is the relative density mismatch between fluid and sediment ($s = 2.65$ for quartz in water). Lastly, the constant parameter $\widehat{\kappa}$ determines the time and spatial scale at which $\widehat{\gamma}$ reaches the equilibrium value $\widehat{\gamma}_{ss}$.

The entrainment form for sediment mass conservation (4) is consistent with novel approaches that consider diffusion to be a key process of sediment transport. New theories incorporating diffusion have been developed in the last decade, proving that the intrinsic particle diffusion arises from the second moment of the probability density function of particle displacements (Furbish et al., 2012b; Ancey and Heyman, 2014; Ballio et al., 2018). The theory also shows that particle advection provokes nonlocal effects, which look like (local) diffusion on the macro-scale (Ancey et al., 2015). On the numerical side, a benchmark analysis of different bedload transport models provides evidence that those including particle diffusion perform better than classic models (Bohorquez and Ancey, 2016).

In (4), the function $\widehat{\gamma}_{ss}$ is conditional because the Shields number must be greater than the critical value Sh_{cr} (threshold of incipient motion) for the solid discharge to be nonzero: $\widehat{\gamma}_{ss} = \text{func}(Sh)$ for $Sh > Sh_{cr}$, but $\widehat{\gamma}_{ss} = 0$ for $Sh \leq Sh_{cr}$. Many equations derived empirically (*e.g.* Meyer-Peter and Müller, 1948; Ackers and White, 1973; Fernandez Luque and van Beek, 1976) are commonly used and provide decent predictions at sufficiently high Shields numbers and over long time-scales (Wu, 2007). Equation (4) describes how sediment particles are advected by the water flow (at velocity $\widehat{\boldsymbol{u}}_p$), spread along the bottom of the channel, and erode or settle depending on the sign of $\widehat{\gamma}^{\varphi}_{ss} - \widehat{\gamma}$. However, this equation does not define the particle transport rate which has no unique expression (Ancey, 2010; Furbish et al., 2012a; Ballio et al., 2018).

Here we borrow from Furbish et al. (2012b) the definition of the mean sediment transport rate $\widehat{\overline{\boldsymbol{q}}}_s$ as the sum of convective and diffusive contributions

$$\widehat{\overline{\boldsymbol{q}}}_s = \widehat{\boldsymbol{u}}_p\,\widehat{\gamma} - \widehat{\alpha}\,\nabla\widehat{\gamma}\,. \tag{6}$$

In the non-equilibrium transport theory, both contributions can be computed by solving the advection-diffusion equation (4) for the mean particle activity $\widehat{\gamma}$. Conversely, in the equilibrium transport approach, one neglects the diffusive flux assuming a uniform flow, which yields $\widehat{\overline{\boldsymbol{q}}}_s = \widehat{\overline{\boldsymbol{q}}}_{ss}$ with

$$\widehat{\overline{\boldsymbol{q}}}_{ss} \equiv \widehat{\boldsymbol{u}}_p\,\widehat{\gamma}_{ss}\,. \tag{7}$$

The function $\widehat{\overline{\boldsymbol{q}}}_{ss}$ is commonly referred to as sediment transport capacity.

Equation (4) also dictates bed evolution when embodied in the Exner equation,

$$(1-\zeta_b)\,\frac{\partial\widehat{z}}{\partial\widehat{t}} = \widehat{\kappa}\,(\widehat{\gamma} - \widehat{\gamma}^{\varphi}_{ss})\;, \tag{8}$$

in which ζ_b is the bed porosity.

The equilibrium transport approach does not require the resolution of (4) because one assumes that the relation $\widehat{\gamma} = \widehat{\gamma}^{\varphi}_{ss}$ also holds under non-uniform flow conditions. Substituting (4) into (8), assuming a slowly varying flow conditions (when $\partial_t\widehat{\gamma} \sim \widehat{\alpha}\nabla^2\widehat{\gamma} \ll \widehat{\kappa}\,\widehat{\gamma}_{ss}$), and setting $\widehat{\boldsymbol{u}}_p\,\widehat{\gamma} = \widehat{\overline{\boldsymbol{q}}}_{ss}$, the Exner equation (8) is cast in the standard form

$$(1-\zeta_b)\frac{\partial\widehat{z}}{\partial\widehat{t}} + \nabla\cdot\widehat{\overline{\boldsymbol{q}}}_{ss} = 0\,. \tag{9}$$

Formally, this approximation is valid in the absence of a strong gradient in the sediment transport rate.

2.3. Capability to predict megaflood-scale dunes and antidunes

The prediction of the occurrence of bedforms and its morphology has been a case study of great interest due to its influence in major geophysical flows such as mega-floods and the effects on the landscape in general. The main theoretical frameworks used to study this problem can be classified, according to the flow equations, into rotational formulations using Navier-Stokes equations, and its depth-integrated form known as the shallow-water equations (also referred to as the Saint-Venant equations). Morphodynamic models add

supplementary equations that describe sediment transport processes, as described beforehand.

Since the earliest attempt by Reynolds (1965), authors have tried to predict the formation of ripple, dune, antidune and cyclic step using reduced-order models as the standard Saint-Venant-Exner equations (e.g., Gradowczyk, 1968; McLean, 1990; Balmforth and Provenzale, 2001). The linear stability analysis unlikely predicts that a uniform flow is unconditionally stable for Froude number, $\mathcal{F}r \equiv |\widehat{\boldsymbol{u}}|/\sqrt{\widehat{g}\,\widehat{\eta}}$, lower than 2, preventing the formation of the desired bedforms. Even if the Exner equation (9) is replaced with a non-equilibrium sediment transport model, bedforms occur only with a Froude number above unity, corresponding with upstream migrating cyclic steps (Balmforth and Vakil, 2012) and antidunes (Deigaard, 2006; Di Cristo et al., 2006; Vesipa et al., 2012; Bohorquez and Ancey, 2015; Greco et al., 2017). Successful morphodynamic models for dune formation based on the Saint-Venant equations are scarce and require an ad-hoc bed slope correction term that triggers the instability of the bed (Nabi et al., 2014; Mendoza et al., 2017).

The Navier-Stokes approach has proven to be a good option to predict with accuracy the growth and evolution of dunes (Dey, 2014, Ch. 8), whose standardised numerical scheme and closure equations provide reliable results checked with experimental data at the laboratory scale (Niemann et al., 2010; Nelson et al., 2016; van Duin et al., 2017; Olsen, 2017; Vellinga et al., 2018). On the theoretical side, the physical problem at hand was recently solved with linear stability theory using a rotational two-dimensional flow model (e.g. Bose and Dey, 2009; Camporeale and Ridolfi, 2011; Andreotti et al., 2012; Charru et al., 2013). The base flow of the water phase was described with a log-law layer over the whole flow depth, a hypothesis that holds for Reynolds number close to 10^4. No consensus exists in this framework regarding the use of the Exner equation (equilibrium theory) or the flux relaxation equation (non-equilibrium sediment transport formulation).

Even though a rotational formulation seems to be a great solution, a subtlety of existing linear stability theories is the use of a Prandtl-like closure and the assumption that the turbulent boundary-layer extends through the whole flow depth, which holds true in the limited range of Reynold numbers $10^{-4} < \mathcal{R}e < 10^{-6}$. That is to say that the outer layer of the turbulent boundary layer was not accounted for. Therefore, such theories cannot be applied directly to megafloods which develop Reynolds numbers several orders of magnitude larger than 10^6, as explained below.

As a matter of fact, the paleohydrology of megafloods is commonly based on the reconstruction of the flow in the outer layer by means of the shallow-water equations (1)-(2). Carrivick (2006) and Winsemann et al. (2016) reported maximum values of depth and velocity of 10-50 m and 10-15 m·s^{-1}, and even higher values of about 550-680 m and 50-60 m·s^{-1} were found in the Missoula (Denlinger and O'Connell, 2010; Alho et al., 2010) and the Altai megafloods (Carling et al., 2010; Bohorquez et al., 2016). Hence, the Reynolds number is about 10^8 in high-magnitude floods and 10^{10} in megafloods. According to Nezu and Nakagawa (1993), for high Reynolds number ($\mathcal{R}e > 2.3 \times 10^4$), the outer layer occupies more than 80 per cent of the flow depth, and the inner layer is confined within less than 20 per cent. Subsequently, this study is motivated by the need to formalise a simple and standard shallow-water theory that accurately and efficiently describes the dune and antidune instability of an erodible bed.

3. Three-dimensional stability diagram of dunes and antidunes

3.1. The classical two-dimensional bedform predictor

The widest accepted stability diagram of the dune-antidune transition was originally proposed by Kennedy (1963). He identified two key nondimensional parameters in his potential flow theory, namely the nondimenional wavenumber, k, and the Froude number, $\mathcal{F}r$, given by

$$k = \frac{2\pi\,\widehat{\eta}_0}{\widehat{\Lambda}}\,, \quad \mathcal{F}r = \frac{\widehat{u}_0}{\sqrt{\widehat{g}\,\widehat{\eta}_0}}\,, \tag{10}$$

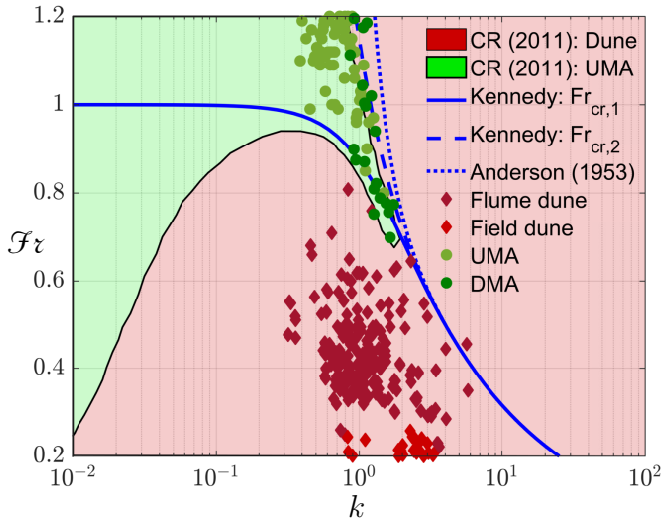

Fig. 2: Standard representation of the regions of dune and antidune in the parameter space $\{k, \mathcal{F}r\}$. Data from sources listed in Carling and Shvidchenko (2002), Cheng (2016), Bradley and Venditti (2017) and Recking et al. (2009).

where $\widehat{\Lambda}$ is the wavelength of the bedform, $\widehat{\eta}_0$ is the flow depth of the uniform stream, $\widehat{u}_0 = |\widehat{\boldsymbol{u}}_0|$ represents the magnitude of the depth-averaged velocity and $\widehat{g}$ denotes the gravitational acceleration. His linear stability theory correctly predicted the transition from dune and antidune observed in experiments as the Froude number increases above the critical value $\mathcal{F}r_{cr,1} = k^{-1/2} \tanh^{1/2} k$. Kennedy prescribed the value of the lag between the bottom shear stress and the flow velocity. In doing so, he improved the prediction of the potential flow theory without phase lag by Anderson (1953) that sets the critical Froude number:

$$\mathcal{F}r_{cr,3} = \left[\frac{\sinh 2\,k}{k\ (\tanh k \sinh 2\,k - 2)} \right]^{1/2} . \qquad (11)$$

Since Kennedy, it is well-known that a lag between the sediment discharge and the bed profile is required in order for the dune instability to take place (McLean, 1990).

We revisited the available experimental data for dunes (Carling and Shvidchenko, 2002; Cheng, 2016; Bradley and Venditti, 2017) and antidunes (Recking et al., 2009), and represented the dataset in the plane $\{\mathcal{F}r\,, k\}$, see Fig. 2. It is readily observed that Kennedy's bedform stability diagram accurately predicts the transition from downstream migrating dune to upstream migrating antidunes. Interestingly, the antidune wavenumber in the experimental dataset at the laboratory scale is confined in the narrow region $0.4 \leq k \leq 1.5$. Assuming $k = 1$ and knowing the antidune wavelength $\widehat{\Lambda}$ from sedimentary records, authors retrodicted the flow depth, $\widehat{\eta}_0 \approx \widehat{\Lambda}/(2\,\pi)$, in paleohydraulic studies with an error lower than 50 % (Shaw and Kellerhals, 1977; Maejima et al., 2009; Carling et al., 2009a; Froude et al., 2017; Carling and Leclair, 2018). Furthermore, the flow velocity is routinely inferred from the condition $\mathcal{F}r \sim 1$, which yields $\widehat{u}_0 \sim [\widehat{g}\,\widehat{\Lambda}/(2\,\pi)]^{1/2}$. The uncertainty in the velocity estimates can be as high as 100 % because antidune may develop with Froude numbers between 0.7 and 2 (Carling and Shvidchenko, 2002), see also Fig. 3a. In the dune case, the wavenumber and the Froude number are poorly constrained in flume experiments (and large-rivers), varying between 0.3-5.6 (0.2-14.2) and 0.22-0.83 (0.1-0.28), respectively.

Using the two-dimensional stability diagram (recall Fig. 2), several authors have proposed alternatives theories for dune formation (e.g. Parker, 1975; Richards, 1980; Nakagawa and Tsujimoto, 1980, 1984; Bose and Dey, 2009; Fourrière et al., 2010; Camporeale and Ridolfi, 2011; Andreotti et al., 2012; Charru et al., 2013). Bose and Dey (2009) accounted both for bedload and washload by incorporating an advection-diffusion equation similar to (4). Later on, the sensitivity of the linear instability results with the sediment transport formulation was explored (Camporeale and Ridolfi, 2011). The comparison between linear stability results and available experiments shows an excellent agreement when using a simplified version of (4) with $\partial_t \langle \gamma \rangle \approx 0$ and $\widehat{\alpha} = 0$, as shown in Fig. 2. The rotational formulation predicts the formation of dune and upstream migrating antidune (UMA) within the regions in red and green depicted, respectively. The black solid line highlights the transition between both bedforms, which nearly overlaps Kennedy's one (blue solid line) and experiments.

Kennedy (1963) also found a second transition above $\mathcal{F}r_{cr,2} = [k \tanh(k)]^{-1/2}$ associated

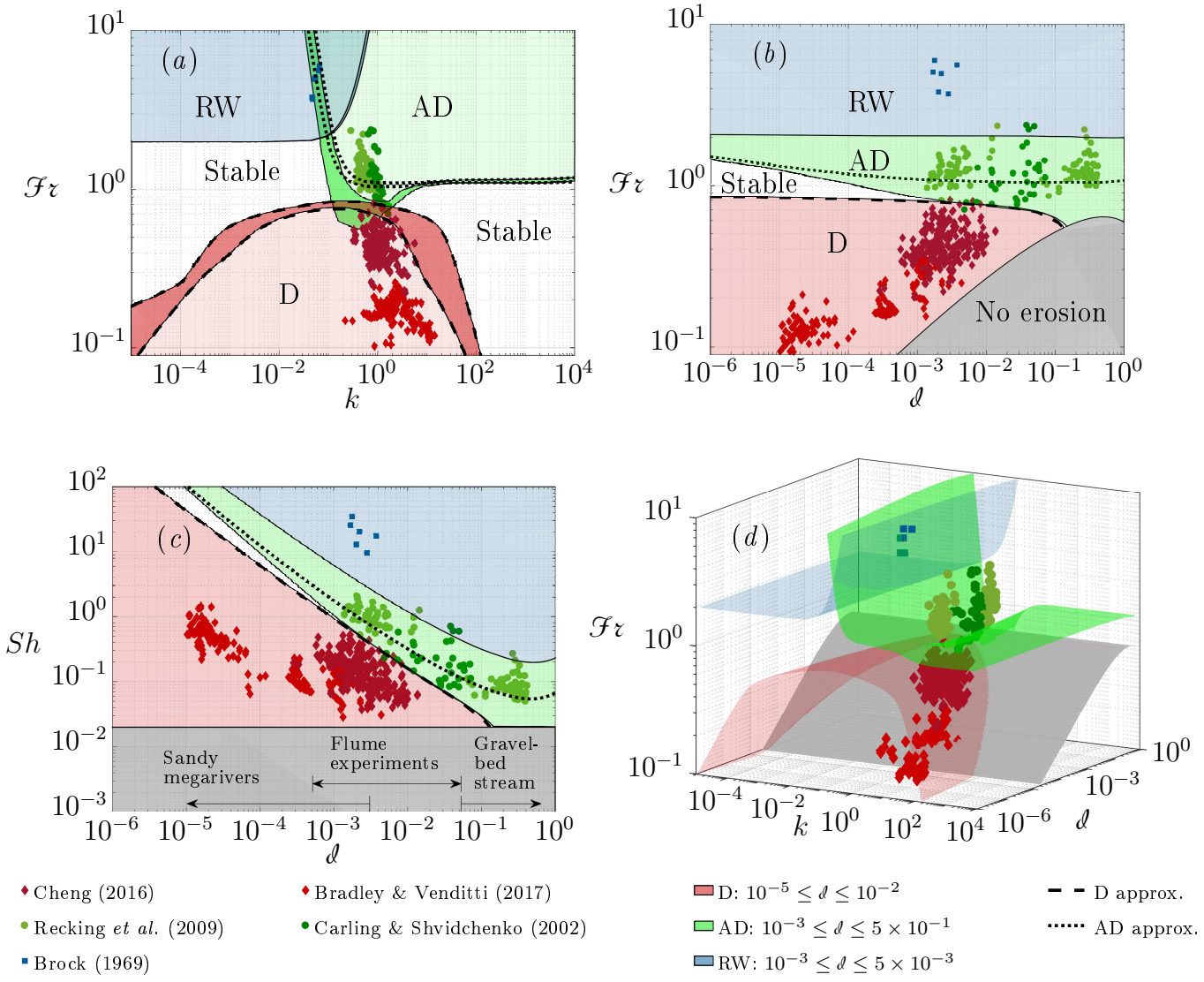

Fig. 3: (*a*) Plan view of the unstable regions in the parameter space $\{k, \mathcal{F}r\}$ associated to the roll wave (RW), dune (D) and antidune (AD). The area described by the neutral curve when ℓ varies in the ranges given in the legend is depicted in dark colour. (*b*) Unstable regions in the parameter space $\{\ell, \mathcal{F}r\}$ for values of k observed in the experiments. No erosion occurs in the light grey area that corresponds with $Sh < Sh_{cr}$. (*c*) Unstable regions in the parameter space $\{\ell, Sh\}$ for the values of k observed in the experiments. (*d*) Three-dimensional view of the neutral surfaces showing that the experimental points lie in the unstable regions. The approximate neutral curves for dune (dashed line) and antidune (dotted line) in panels a, b and d were evaluated by setting $\lambda = 0$ with $U \approx 0$ in (25). The supplementary movie 1 shows a rotating view of the neutral surfaces and its corresponding approximate solution.

with downstream migrating antidunes (DMA). However, recent investigations have demonstrated that the direction of migration of the antidune is determined by the two possible non-linear states of the water surface for the same shape of the bed (Baines and Whitehead, 2003). Deigaard (2006) used non-linear numerical simulations, while Núñez-González and Martín-Vide (2011) worked out analytical solutions to prove this result. In the DMA regime, the water depth is less over the crest than over the trough and, in UMA, the water depth is greater over the crest than over the trough. Hence, a linear stability theory cannot be used to determine the downstream or upstream migration of the antidune.

3.2. The third dimension: the grain roughness

Carling and Shvidchenko (2002) highlighted the

relevance of the grain size on the dune-antidune transition, allowing the definition of a third, crucial, nondimensional parameter. In their seminal work, they accounted for the relative depth, which is defined as the ratio of the flow depth $\widehat{\eta}_0$ to the mean diameter of the grains $\widehat{d}$. Alternatively, we use in this review the inverse of the relative depth, i.e. the relative grain roughness, given by

$$\ell = \frac{\widehat{d}}{\widehat{\eta}_0} \,. \tag{12}$$

The relative grain roughness is a key parameter in the evaluation of the hydraulic resistance (3) and, subsequently, cannot be ignored (García, 2007; Julien, 2010). Unfortunately, as Kennedy did not account for the effects of the sediment roughness, and the two-dimensional diagram in Fig. 2 has become a standard, most theoretical studies do not include the influence of the relative depth or grain roughness.

Inspired by Carling and Shvidchenko (2002), we draw the experimental data in the planes $\{k, \mathcal{F}_\tau\}$ (Fig. 3a) and $\{\ell, \mathcal{F}_\tau\}$ (Fig. 3b). For the sake of the completeness, we included the experiments by Brock (1969) for roll waves in a fixed bed. The grain roughness relative to flow depth, ℓ, extends in our study from characteristic values of large sandy rivers ($10^{-5} < \ell < 3\times10^{-3}$) to flume experiments ($5 \times 10^{-4} < \ell < 5 \times 10^{-2}$) and gravel-bed rivers ($\ell > 5 \times 10^{-2}$). The corresponding value of the Froude number monotonously increases with ℓ from $\mathcal{F}_\tau \approx 0.1$ (large sandy river) to $\mathcal{F}_\tau \approx 2$ (gravel-bed river).

The diagram $\{\ell, \mathcal{F}_\tau\}$ (Fig. 3b) depicts a sharp border between dune and antidune for flume experiments. As reported by Carling and Shvidchenko (2002), the Froude number varies within $0.7 < \mathcal{F}_\tau < 0.8$ for $5 \times 10^{-4} < \ell < 5 \times 10^{-2}$ in the thin area where both bedforms coexist. Roll waves may develop with similar roughness but at the higher Froude numbers $2 < \mathcal{F}_\tau < 6$. On the contrary, if the Froude number is low, no erosion occurs (gray area in Fig. 3b) due to the general threshold condition for incipient motion $Sh > Sh_{cr} = 0.02$ (Julien, 2010). Exceptional downstream migrating antidunes occur when the roughness increases to $10^{-2} < \ell < 10^{-1}$, recovering the upstream migrating direction with a higher roughness ($\ell > 10^{-1}$). No dunes have been observed with these roughness values. In the opposite limit, deep flows as large rivers and megafloods induce much smaller values of the relative roughness ℓ (12) because this parameter represents the inverse of the relative depth. In gauged large sandy rivers with $\ell < 10^{-3}$, only dunes have been observed (Bradley and Venditti, 2017). The analysis of Fig. 3b reveals that dunes essentially cannot form in gravel-bed streams, and in-situ measurements of antidunes have not been conducted in large rivers.

To draw an explanation, we shall use a bedform diagram similar to Julien and Raslan (1998), see Fig. 3c, where we plot the Shields number (originally, the transport-stage parameter) as a function of the relative roughness (i.e. the inverse of the relative submergence). Taking into account that a steady, uniform state was achieved in the flows analysed in Fig. 3, mapping $\mathcal{F}_\tau$ to Sh is straightforward by substituting (3), (10) and (12) into (5),

$$Sh = \frac{f\,\mathcal{F}_\tau^{\,2}}{8\,(s-1)\,\ell} \,. \tag{13}$$

Interestingly, the Shields number for dunes is higher in large rivers ($0.06 \leq Sh \leq 1.4$) than in flume experiments ($0.03 \leq Sh \leq 0.5$), even when the corresponding Froude number is much lower at the laboratory scale ($0.1 \leq \mathcal{F}_\tau \leq 0.28$ and $0.22 \leq \mathcal{F}_\tau \leq 0.83$, respectively). The absence of antidunes in large sandy rivers can be understood by the small velocity of the large rivers measured by Bradley and Venditti (2017) so that the flow becomes subcritical. The maximum value of the Shields number was $Sh = 1.4$ for $\mathcal{F}_\tau = 0.18$ and $\ell = 1.5 \times 10^{-5}$, while laboratory experiments exhibit the lower maximum $Sh = 0.5$ for $\mathcal{F}_\tau = 0.72$ and $\ell \approx 10^{-3}$. The highest Shields number in deep flows are so notable that, at the laboratory scale, larger values (i.e. $Sh > O(1)$) would lead to upper-stage plane bed (Carling, 1999).

Upstream-migrating antidunes have bed monitored in gravel-bed streams both at the laboratory scale (Recking et al., 2009) and real rivers on steep slopes (Froude et al., 2017). Characteristic values of Shields, Froude and dimensionless

Fig. 4: Train of nine antidunes observed during a flash flood in the gravel-bed Belham river (West Indies). See also Video Clip S2 in Froude et al. (2017).

roughness are $0.05 \leq Sh \leq 0.27$, $0.9 \leq \mathcal{F}_\ell \leq 2.2$ and $\delta \geq 0.1$, respectively, as shown in Figs. 3b-c. Dunes cannot form if the sediment is very coarse (or the flow is very shallow) because antidunes will form instead, the flow being close to critical speed.

Carling et al. (2009a) pointed out that the condition for the preservation of antidunes is less well understood. A putative explanation based on Fig. 3c is that the corresponding Shields number for a megaflood ($\delta < 10^{-4}$) is so high for Froude numbers larger than the antidune threshold ($\mathcal{F}_\ell \sim 0.7 - 0.8$) that bedforms would be washed out under a steady, uniform flow. To remain below the threshold for upper-stage plane bed, one thus requires an unsteady flow in which the Shields number is independent of the Froude number. This fact may explain why antidune paleostage indicators are so scarce. A limited number of sedimentary records exist, namely: 60-90 m wavelength standing waves in the Middle Pleistocene Emme delta (Winsemann et al., 2011), several wave trains in the Camas Prairie Basin (Lake Missoula, Montana, US) are 91 m from crest to crest (Pardee, 1942), see Fig. 1c, and gravelly antidunes in glacifluvial Gilbert-type deltas are 10 m length (Lang et al., 2017), among other lesser scale examples. The coexistence of antidunes with other supercritical bedforms in the geological record supports the paleoflood reconstruction method based on the assumption of a critical Froude number outlined in Section 3.1 (see also Carling et al., 2009b). For instance, Grant (1994) demonstrated that wave trains of antidunes coarsen as they collide with one another and merge, as illustrated in figure 4, and may lead to step pools. Antidunes downstream erosional steps (Winsemann et al., 2011) and sandy cyclic steps (Lang et al., 2017) have also been reported.

Finally, we originally plot the available data on the three-dimensional parameter space $\{k, \delta, \mathcal{F}_\ell\}$ in Fig. 3d. Rotating views of the new diagram can be watched in the Supplementary video 1. It is worth noting that the standard two-dimensional representation by Kennedy (recall Figs. 2 and 3a) is a simple projection of the three-dimensional points $\{k, \delta, \mathcal{F}_\ell\}$ onto the plane $\{\mathcal{F}_\ell,\ k\}$. The information relative to the flow depth or grain size is lost. Therefore, the original bedform predictor by Kennedy is only reliable for shallow-flow laboratory experiments where both dune and antidune may develop. However, it deviates from observed bedforms in large sandy rivers and gravel-bed streams where only dune and antidune exist, respectively. The influence of the relative roughness δ cannot be neglected. Similarly, the alternative view in Fig. 3b represents the projection of the three-dimensional bedform stability diagram onto the plane $\{\mathcal{F}_\ell,\ \delta\}$ losing the information relative to the wavelength. Formally, we can fix a constant value of δ and draw a bedform stability diagram in the plane $\{\mathcal{F}_\ell,\ k\}$. Such a plot is sensitive to the relative roughness δ and, consequently, its dependency should be retained, as shown in Section 4.4.

The remaining of this review aims at formulating a shallow-water theory that can reproduce the three-dimensional bedform stability diagram shown in Fig. 3d and retrieve the two-dimensional representations by Kennedy (1963) and Carling and Shvidchenko (2002) shown in Figs. 3a-b as a projection of the three-dimensional space onto two dimensions (Section 4). Then, we show the applicability of the nondimensional bedform diagrams to predict the formation of giant dunes and antidunes using as input parameters the reconstructed values of the hydraulic variables in the Altai and Missoula floods, respectively (Section 5).

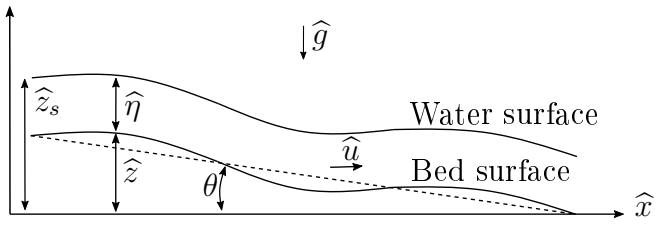

Fig. 5: Sketch of an open channel flow over an erodible bed.

4. Linear stability theory for the formation of dune and antidune

4.1. Nondimensional control parameters

To formulate a theory for the nondimensional stability diagrams depicted in Figs. 2-3, the first step is to make the model equations dimensionless. Then, we identify the set of nondimensional parameters that appear in the resulting equations and formulate appropriate closure laws in terms of the control parameters (i.e. $\mathscr{d}$ and $\mathcal{F}\mathscr{r}$, alternatively Sh).

With a suitable scaling with respect to a length scale $\widehat{\eta}_0$, a velocity scale $\widehat{u}_0$, and a characteristic particle activity $\widehat{\gamma}_0$ (solid volume of particles in motion per unit streambed area), corresponding to a one-dimensional uniform flow (see sketch in Fig. 5), the Saint-Venant-Exner equations (1)-(8) can be rendered dimensionless. The subscript 0 denotes the value of the base flow from now on. The governing equations of the water depth, $\eta(x,t)$, and speed, $u(x,t)$, the height of the bed, $z(x,t)$, and the mean particle activity, $\gamma(x,t)$, can be written in the dimensionless form

$$\frac{\partial \eta}{\partial t} + \frac{\partial \eta u}{\partial x} = 0\,, \tag{14}$$

$$\mathcal{F}\mathscr{r}^2\left[\frac{\partial \eta u}{\partial t} + \frac{\partial \eta u^2}{\partial x} - \nu\frac{\partial}{\partial x}\left(\eta\frac{\partial u}{\partial x}\right)\right] + \eta\frac{\partial \eta}{\partial x} = -\eta\frac{\partial z}{\partial x} - \mathcal{F}\mathscr{r}^2\frac{f}{8}u^{\varphi 2}\,, \tag{15}$$

$$\frac{\partial z}{\partial t} = \kappa_\gamma\left(\gamma - \gamma_{ss}^{\varphi}\right)\,, \tag{16}$$

$$\frac{\partial \gamma}{\partial t} + \beta\frac{\partial u\gamma}{\partial x} - \alpha\frac{\partial^2 \gamma}{\partial x^2} = \kappa_\eta\left(\gamma_{ss}^{\varphi} - \gamma\right)\,, \tag{17}$$

representing the mass (14) and momentum (15) conservation of the water flow, the Exner equation tracking the bed-stream interface (16), and the mass conservation for bedload (17). The dimensionless parameters are the Froude number, $\mathcal{F}\mathscr{r}$, an eddy viscosity, ν, the Darcy-Weisbach friction factor, f, the dimensionless deposition rates, κ_η and κ_γ, the sediment-to-water velocity ratio, β (≤ 1), and the particle diffusivity, α. They are related with the dimensional quantities (denoted below by a circumflex) by means of the following scales:

$$\begin{aligned} \nu &= \frac{\widehat{\nu}}{\widehat{\eta}_0\,\widehat{u}_0}\,, \quad \kappa_\eta = \frac{\widehat{\kappa}\,\widehat{\eta}_0}{\widehat{u}_0}\,, \\ \kappa_\gamma &= \frac{\widehat{\kappa}\,\widehat{\gamma}_0}{(1-\zeta_b)\,\widehat{u}_0}\,, \quad \alpha = \frac{\widehat{\alpha}}{\widehat{\eta}_0\,\widehat{u}_0}\,. \end{aligned} \tag{18}$$

For the sake of the brevity, only the novel closure law for the phase lag is introduced below. The rest of mathematical expressions, which are used to evaluate $\{f,\ \nu,\ \beta,\ \alpha,\ \kappa_\gamma,\ \kappa_\eta,\ \gamma_{ss}\}$ as a function of $\{\mathscr{d}, \mathcal{F}\mathscr{r}\}$, are given in Appendix A.

A new ingredient in this work is the adoption of a simple friction force equation in (15) valid to model the effects of the thin shear layer over an erodible wavy bottom. The hydraulic resistance is based on the well-known Darcy-Weisbach friction factor, f, and a phase lead, φ, developing between the bottom shear stress and the mean velocity, which is evaluated as $u^{\varphi}(x,t) = u(x+\varphi/k,t)$. Recall that the superscript φ is used to identify the lagged terms in the current review paper.

Most experimental results focused on characterising the bedform dimensions, and less attention was paid to the phase lag, φ. Recently, Heyman, Bohorquez and Ancey (2016) measured the shear stress distribution in laboratory experiments on shallow supercritical flow on a sloping mobile bed, getting $\varphi = 0$ in the antidune regime. As a matter of fact, antidune is commonly referred to as in-phase wave (Carling and Shvidchenko, 2002; Recking et al., 2009). Conversely, experiments with fixed dune-like features have shown that the phase lag can reach a maximum of $\pi/2$ (Frederick and Hanratty, 1988). Setting the threshold $\mathcal{F}\mathscr{r} \approx 0.7$ for the occurrence of antidunes (Carling and Shvidchenko, 2002), see also Fig. 3, and taking into account that only dune (antidune) occurs for $\mathscr{d} \leq 10^{-3}$ ($\mathscr{d} > 10^{-2}$), we have proposed

the empirical relation

$$\varphi(\mathcal{F}\mathfrak{r}, \ell) = \frac{\pi}{4}\left[1 - \tanh(10\,\mathcal{F}\mathfrak{r} - 7)\right] \exp(-7.36\,\ell)\,. \tag{19}$$

Note that φ tends to $\pi/2$ for $\ell < 10^{-2}$ and $\mathcal{F}\mathfrak{r} < 0.7$, vanishing otherwise.

4.2. Eigenvalue problem

The conditions required for a disturbance to grow over a flat erodible bed and form a large bedform can be established using a linear stability theory (see the review by McLean, 1990). In a temporal, linear stability analysis the unknowns are eventually the temporal frequency and the growth rate of the perturbation, denoted here by ω_r and ω_i, respectively. Both unknowns depend on the wavenumber, k, and the control parameters $\{\ell,\ \mathcal{F}\mathfrak{r}\}$ through an equation denominated dispersion relation and the closure laws outlined in Section 4.1, as further developed below. The sign of ω_r determines whether the perturbation moves downstream ($\omega_r > 0$, i.e. dune) or upstream ($\omega_r < 0$, i.e. antidune). Furthermore, the nondimenional wave speed of the disturbance, given by $c = \omega_r/k$, establishes whether it moves faster than the base flow ($c > 1$). Commonly, a linear stability theory is formulated in complex variables, allowing to write a single complex equation, i.e. the dispersion relation, for the unknown complex frequency, $\omega = \omega_r + \mathrm{i}\,\omega_i$, as a function of the real wavenumber k (Schmid and Henningson, 2001).

The dispersion relation was derived by setting the determinant of the stability matrix (20) to zero, i.e. $\mathbb{D}(k,\omega) \equiv |\mathbf{A}| = 0$. The derivation of the stability matrix is given in Appendix B. The ensuing equation links the real wavenumber, k, with the complex frequency, ω. The base flow is unstable (stable) when the growth rate is positive $\omega_i > 0$ (negative $\omega_i < 0$). Also, it serves to obtain the neutral curve ($\omega_i = 0$), which determines the conditions for the growth of linear instabilities.

$$\mathbf{A} \equiv \left[\mathrm{i}\,k \begin{pmatrix} \beta & \beta \\ \mathrm{i}\,\kappa_\gamma\,\omega^{-1} & \mathcal{F}\mathfrak{r}^2 - \mathrm{i}\,\kappa_\gamma\,\gamma'_{ss}\,\omega^{-1}\exp(\mathrm{i}\,\varphi) - k\,(k-\omega)^{-1} \end{pmatrix} - \mathrm{i}\,\omega \begin{pmatrix} 1 & 0 \\ 0 & \mathcal{F}\mathfrak{r}^2 \end{pmatrix} - k^2 \begin{pmatrix} -\alpha & 0 \\ 0 & -\mathcal{F}\mathfrak{r}^2\,\nu \end{pmatrix} + \begin{pmatrix} \kappa_\eta & -\kappa_\eta\,\gamma'_{ss}\exp(\mathrm{i}\,\varphi) \\ 0 & 2\,S\exp(\mathrm{i}\,\varphi) + k\,S\,(k-\omega)^{-1} \end{pmatrix}\right]. \tag{20}$$

The stability matrix $\mathbf{A}$ can be utilized for establishing the relative importance of the lagged terms arising from the shear stress contribution, $L_S = 2\,S\exp(\mathrm{i}\,\varphi)$ in (20), and its entrainment rate counterparts, $L_\gamma = k\,\kappa_\gamma\,\gamma'_{ss}\,\omega^{-1}\exp(\mathrm{i}\,\varphi)$ in (20). Using (A.4)-(A.5) and the closure law of κ_γ given in Appendix A, we arrive at $L_S/L_\gamma = 0.92\,\mathcal{F}\mathfrak{r}\,\ell^{1/2}\,\omega/k$. Dunes in Fig. 3 occur at $\{\mathcal{F}\mathfrak{r} < 0.7,\ \ell < 10^{-2}\}$ and move with wave speed $c = \omega_r/k < 0.1$, which yields $L_S/L_\gamma < 6\times10^{-3}$ near criticality ($\omega_i \approx 0$), allowing us to neglect the phase lag of the shear stress with respect to its effect on the entrainment rate, i.e. $L_S \approx 2\,S$. We used this approximation in the solution of the eigenvalue problem shown in Fig. 3, and verified the negligible influence of the phase lag on the hydraulic resistance term by comparing the solutions with $L_S = 2\,S$ and $L_S = 2\,S\exp(\mathrm{i}\,\varphi)$ in Section 4.4.

4.3. Analytical solution of bedform growth rate and wave speed

Following the earlier work of Kennedy (1963, 1969), we can work out an approximate, closed-form solutions for the growth rate, λ, and wave speed, U, of the bedform. These are an approximation to the solution of the full eigenvalue problem with $\lambda \approx \omega_i$ and $U \approx \omega_r/k$. The main advantage of Kennedy's approach is the provision of algebraical expressions of λ and U, which cannot be derived from the dispersion relation. However, it involves a hypothesis referred to as quasi-steady

assumption which needs to be verified, as done in this paper.

Travelling-wave solutions to the conservation laws (14)–(17) are sought for a bedform moving downslope with speed U. A wavefront-centred coordinate system is introduced by the transformation ($\xi = x - U\,t$, $\tau = t$). Hence, the system is reduced to the following

$$\frac{\partial}{\partial\xi}\left[\eta\,(u-U)\right] = 0\,, \tag{21}$$

$$\frac{\partial}{\partial\xi}\left[\mathcal{F}\mathfrak{r}^2\eta u\,(u-U) + \frac{\eta^2}{2} - \mathcal{F}\mathfrak{r}^2\nu\eta\frac{\partial u}{\partial\xi}\right] = -\eta\frac{\partial z}{\partial\xi} - \mathcal{F}\mathfrak{r}^2\frac{f}{8}u^2\,, \tag{22}$$

$$\frac{\partial z}{\partial\tau} - U\frac{\partial z}{\partial\xi} = \kappa_\gamma\,(\gamma - \gamma_{ss}^{\varphi})\,, \tag{23}$$

$$\frac{\partial}{\partial\xi}\left[(\beta u - U)\gamma - \alpha\frac{\partial\gamma}{\partial\xi}\right] = \kappa_\eta\,(\gamma_{ss}^{\varphi} - \gamma)\,. \tag{24}$$

To make the analytical treatment more feasible, and according with the analysis of the stability matrix **A** (20), we neglected the effects of the phase lag in the momentum equation (22). In addition, we borrowed the quasi-steady assumption from Kennedy (1963) by neglecting $\partial\eta/\partial\tau$, $\partial u/\partial\tau$ and $\partial\gamma/\partial\tau$ with respect to $\partial z/\partial\tau$. This hypothesis has become standard in morphodynamics (Seminara, 2010; Charru et al., 2013). We shall check its accuracy with the linear stability result of the whole eigenvalue problem (Section 4.2).

Equations (21)-(24) can be linearised to study the dynamical response of the flow to an infinitesimal bed perturbation. Then, it is possible to integrate them analytically using the intricate method developed in Appendix C, which yields the algebraic expressions of λ and U that follow

$$\lambda = k^2\,\kappa_\gamma\,(U-1)\,\left[\beta\,N_i - \gamma'_{ss}\,N_c\,\cos(\varphi) - \gamma'_{ss}\,k\,N_s\,\sin(\varphi)\right]/D_e\,, \tag{25}$$

$$U = -k\,\kappa_\gamma\,(U-1)\,\left[\beta\,N_i + \gamma'_{ss}\,k\,N_s\,\cos(\varphi) + \gamma'_{ss}\,N_c\sin(\varphi)\right]/D_e\,, \tag{26}$$

$$N_i = \alpha\,k^2 S\,(3-2U) + \kappa_\eta\,S\,(3-2U) - \alpha\,\mathcal{F}\mathfrak{r}^2\,k^4\,\nu\,(U-1) + k^2\left[\mathcal{F}\mathfrak{r}^2\,(U-1)^2 - 1\right](U-\beta) - \mathcal{F}\mathfrak{r}^2\,k^2\,\kappa_\eta\,\nu\,(U-1)\,, \tag{27}$$

$$N_c = \left[\mathcal{F}\mathfrak{r}^2\,(U-1)^2 - 1\right]\,\left[\alpha^2\,k^4 + \alpha\,k^2\,\kappa_\eta + k^2\,(U-\beta)^2\right] + \kappa_\eta\,\left[S\,(3-2\,U) - \mathcal{F}\mathfrak{r}^2\,k^2\,\nu\,(U-1)\right]\,(U-\beta)\,, \tag{28}$$

$$N_s = \left[\alpha^2\,k^2 + \alpha\,k + (U-\beta)^2\right]\,\left[S\,(2\,U-3) + \mathcal{F}\mathfrak{r}^2\,k^2\,\nu\,(U-1)\right] + \kappa_\eta\left[\mathcal{F}\mathfrak{r}^2\,(U-1)^2 - 1\right](U-\beta)\,, \tag{29}$$

$$D_e = \left[\alpha^2\,k^4 + k^2\,(U-\beta)^2 + 2\alpha\,k^2\,\kappa_\eta + \kappa_\eta^2\right]\left\{S^2\,(3-2U)^2 + k^2 + \mathcal{F}\mathfrak{r}^4 k^2\,(U-1)^4 + \mathcal{F}\mathfrak{r}^4\,k^4\,\nu^2\,(U-1)^2 + 2\,\mathcal{F}\mathfrak{r}^2\,k^2\,(U-1)\left[1 - U + S\,(2U-3)\,\nu\right]\right\}. \tag{30}$$

Recall that the closed-form solutions of the growth rate (25) and wave speed (26) are an approximation to the eigenvalue of the erodible bed instability in (20) with $\lambda \approx \omega_i$ and $U \approx \omega_r/k$. A constraint required for the equivalence of models is the validity of the steady-state approximation in (24) concerning (23), i.e. $\partial z/\partial\tau \ll \partial\gamma/\partial\tau$. Subsequently, one needs $\kappa_\gamma \ll \kappa_\eta$ or, using (18), $\widehat{\gamma}_0 \ll \widehat{h}_0$, that reads as the dilute sediment condition.

4.4. Results

Our theory successfully captures the formation of bedforms described in Sections 3.1 and 3.2. Setting $\omega = \omega_r$ in (20), i.e. $\omega_i = 0$, we solved the dispersion relation for the temporal frequency, ω_r, and the wavenumber, k, by varying the Froude number, $\mathcal{F}\mathfrak{r}$, and the grain roughness, ℓ. The projection of the theoretical neutral surfaces (see

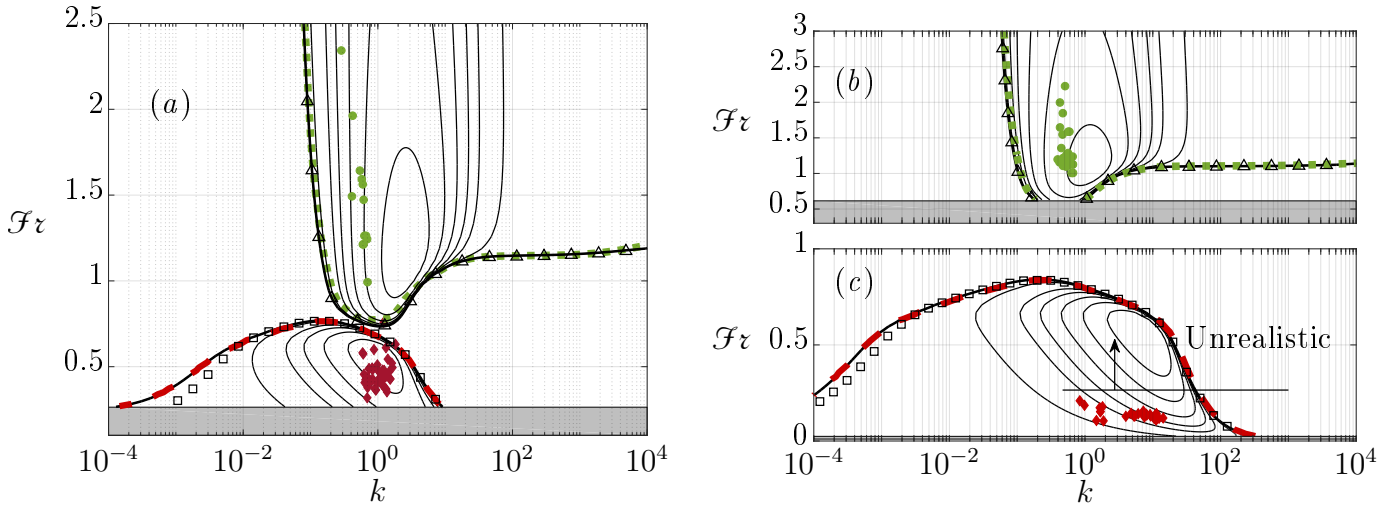

Fig. 6: The contour lines of the constant growth rate in the $\{k, \mathcal{F}r\}$-plane for (a) $\ell = 10^{-2}$, (b) $\ell = 3 \times 10^{-1}$ and (c) $\ell = 2 \times 10^{-5}$ corresponding to flume experiments, gravel-bed streams and large sandy rivers, respectively. The thick solid line shows the neutral curve from the eigenvalue problem (20) neglecting the phase lag in the hydraulic resistance term. The agreement with the true solution (shown with squares and triangles for dune and antidunes, respectively) confirms the validity of the approximation. The dashed and dotted lines depict the analytical neutral curve, i.e. $\lambda = 0$ in (25), for dune and antidune, respectively, with $U \neq 0$ given by (26). Thin contour lines: $\omega_i = 0.001$, 0.005, 0.01, 0.02, 0.04, 0.08 for antidunes and one fourth of these values for dunes.

red, green and blue surfaces in Fig. 3d) onto the $\{k, \mathcal{F}r\}$-plane (see Fig. 3a) shows that experimental data lie within the unstable region for the developments of bedform (dune and antidune) and free-surface instability (roll wave). The representation in Fig. 3a has become a standard in previous linear stability studies, but we strengthen the influence of ℓ on the neutral curve as this point has not been considered in detail beforehand. The areas swept by the neutral curve when ℓ varies in the ranges of $[10^{-5}, 10^{-2}]$ and $[10^{-3}, 0.5]$ for dune and antidune, respectively, are highlighted in dark red and dark green colours.

Different regions of instability arose in laboratory experiments and real scale rivers. To illustrate this point, we found necessary to represent the results as a function of ℓ (see Figs. 3b-d). For $\ell \leq 10^{-3}$, only dune occurs. For $10^{-3} < \ell \leq 10^{-2}$, both dunes and antidunes exist depending on the value of the Froude number. The theoretical transition from dune to antidune regime agrees with existing experimental and field data. At higher values of $\ell > 10^{-2}$ only antidune develops. We consider that the plots in Fig. 6 are more precise than Fig. 3a because they depict the neutral curve (thick solid line) and experimental data (symbol) for a precise value of ℓ. The current theory predicts the formation of both dune and antidune at the laboratory scale (Fig. 6a), only antidune in the gravel-bed stream (Fig. 6b) and dune in large rivers (Fig. 6c). Fig. 6 also depicts with triangles and squares the results of the antidune and dune, respectively, arising from the complete stability matrix (20). In the antidune regime, the solutions overlap because of the obvious reason that φ (19) vanishes. In the dune regime, the agreement is good, corroborating the negligible influence of φ on the shear stress term, L_S, with respect to the entrainment rate counterpart, L_γ.

Interestingly, in our formulation the lag φ produces a growth of the bed perturbations at subcritical Froude numbers even in the absence of diffusion, see Fig. 7a, while in the classic Saint-Venant-Exner analysis it induces damping (e.g. Balmforth and Provenzale, 2001, Section 15.7). Furthermore, the comparison of the contour lines of the constant growth rate with (Fig. 6a) and without (Fig. 7a) diffusion illustrates that diffusivity plays a damping role in the short-wavelength range. If $\nu_t > 0$, the an-

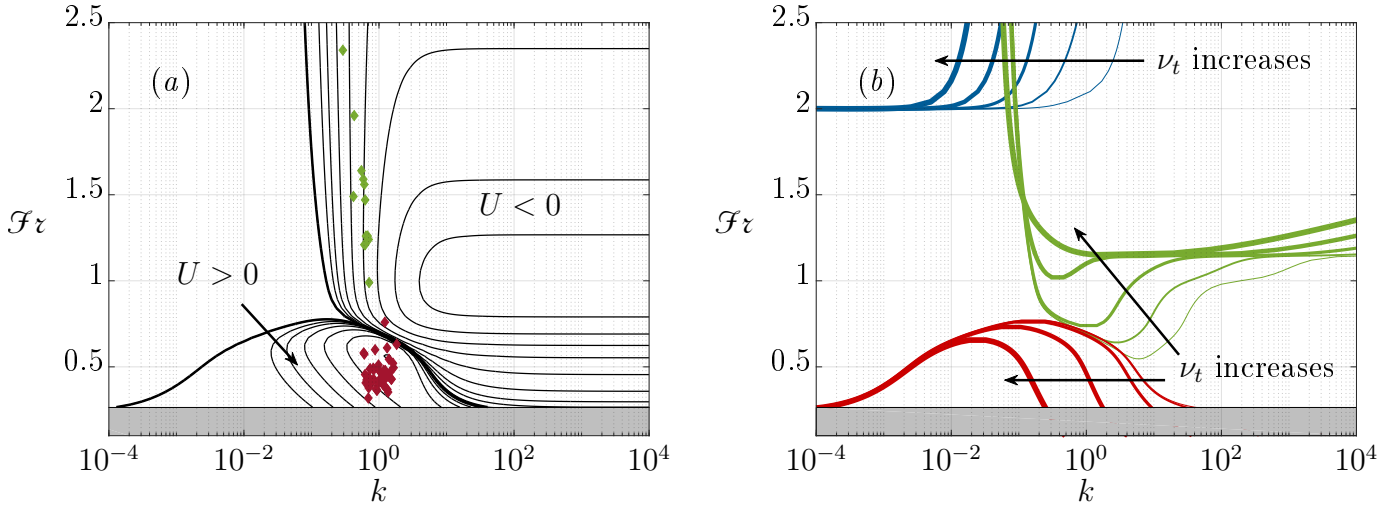

Fig. 7: (a) The contour lines of the constant growth rate in the $\{k, \mathcal{F}r\}$-plane for $\ell = 10^{-2}$, as in Fig. 6a, but setting $\nu_t = 0$ (i.e. $\alpha = \nu = 0$). Thin contour lines: ω_i increases in powers of two from 0.0025 to 0.32 for antidunes ($U < 0$) and from 6.25×10^{-4} to 0.02 for dunes ($U > 0$). (b) Sensitivity of the neutral curve of the dune (red line), antidune (green line) and roll wave (blue line) to variations of ν_t, in powers of ten from 10^{-2} to 10^2, keeping the rest of parameters as in panel a.

tidune growth rates exhibit a maximum near the experimental data. Also, the growth rates acquire a cut-off with $\mathcal{F}r < 1$ that limits the range of unstable wavenumbers, which decreases when ν_t rises. The short-wavelength range can thus be stabilised by increasing the viscosity ν_t, as shown in Fig. 7b. The marginal curves of the dune and roll wave shift to lower wavenumbers, and the critical Froude number of the antidune instability increases becoming supercritical for $\nu_t \approx 10$. We conclude by recalling that erosion-deposition morphodynamic models with $\varphi = 0$ do not capture the formation of dune because the bed disturbance moves always upstream (Bohorquez and Ancey, 2015).

The fact that experimental points lie near the maximum of the growth rate in the antidune case (Figs. 6a-b) implies an absolute instability (Bohorquez and Ancey, 2015, 2016). A system which is absolutely unstable responds selectively to perturbations, and its response is dominated by the mode with zero group velocity, which grows in place, while the other modes are swept away by the flow (Schmid and Henningson, 2001). Using a spatio-temporal stability analysis (i.e. both k and ω are complex numbers), Bohorquez and Ancey (2016, Section 3.3) ensured the existence of saddle points for antidunes by checking the zero group velocity condition, i.e. $c_g = \partial\omega/\partial k = (\partial\mathbb{D}/\partial k)/(\partial\mathbb{D}/\partial\omega) = 0$. It is referred to as the Briggs-Bers or (in Soviet literature) the Fainberg-Kurilko-Shapiro criterion, see Schmid and Henningson (2001). Subsequently, the unrealistic, high wavenumber of the antidune mode ($k \gg 1$) will not manifest because of the existence of a maximum growth rate at a realistic, longer wavelength with zero group velocity. Conversely, the dune is a convective instability that does not satisfy the Briggs-Bers criterion for the existence of an absolute instability.

At this point, we highlight that the approximate solutions of the neutral curves for the dune (dashed line) and antidune (dotted line) superimpose on the complete solution (thick solid line) in Fig. 6. Such a result corroborates that the closed-form solution (25)-(30) converges to that of the full eigenvalue problem (20) near criticality. Furthermore, it is strong evidence for the validity of the quasi-steady hypothesis introduced by Kennedy (1969) and later used by several authors (Seminara, 2010; Charru et al., 2013).

To conclude, we test the simplification $U \approx 0$ in the evaluation of (25). We found that the approximate neutral curve of the antidune does not

overlap when $\mathcal{F}\tau < 1$, as shown in Fig. 3 and the Supplementary movie 1. It follows that the celerity of the morphodynamic response is not negligible for the antidune.

5. Application to megafloods

At this point, we have already proposed a shallow-water formulation that captures the formation of bedforms observed in gravel-bed streams, flume experiments and large rivers. All the experimental data used to verify the linear stability results are based on well-controlled conditions that allowed the evaluation of $\mathcal{F}\tau$, Sh and ℓ from in-situ measurements of hydraulic variables. Mega-floods prevent direct measurements of the peak water discharge, flow depth and velocity (Baker, 1987). Subsequently, megaflood-scale dunes and antidunes are (apparently) not represented in the bedform diagrams (Figs. 3, 6 and 7).

The proposed stability diagram provides a tool to quickly determine potential scale effects in studies of dune-antidune formation by simply plotting the values of $\{\mathcal{F}\tau, \ell\}$ or $\{Sh, \ell\}$ for model and prototype conditions. Here we refer the experiments measured in situ, at the laboratory or real river, as a prototype. The model consists of the megaflood, which hydraulic variables have to be reconstructed using paleohydrology (see Section 2.1). To satisfy the similarity between sediment transport processes in a megaflood model, we need identical values of nondimensional parameters $\mathcal{F}\tau$, Sh and ℓ (Parker et al., 2003; Wilkerson and Parker, 2011). If this condition is true, sediment transport conditions and the associated bed morphology in prototype should precisely reproduce model conditions.

In the next sections, we analyse the reconstructed values of the nondimensional parameters for giant gravel dunes and antidunes sculpted by the Late Pleistocene Altai and Missoula megafloods, respectively.

5.1. Antidunes in the Camas Prairie

5.1.1. Study site

Camas Prairie provides a unique field laboratory on Earth for analysing the formation of large antidunes (Baker, 1973, 2009). These bedforms have a low preservation potential because any progressive deceleration of the flow will cause a plane bed, provoking the destruction of the antidune (Carling et al., 2009a). However, Lister (1981, https://scholarworks.umt.edu/etd/7435) originally found an antidune deposit exposed in a gravel pit on the north side of the Markle Pass (see location map in Fig. 1c) associated to the largest Glacial Lake Missoula draining (Alho et al., 2010). Later, Lee (2009, https://inside.mines.edu/UserFiles/File/Geology/Camas_red.pdf) positioned and characterised with GPS the dimensions of trains of antidunes in three additional Passes (referred to as Big Creek, Wills Creek and Duck Pond). Based on Lee's work, the interpretation of high-resolution orthophotos and a digital elevation model, we delimited in Fig. 1c the areas where antidune formed. For the sake of the completeness, fields of giant ripples and reverse dunes are also highlighted.

In the Wills Creek, Big Creek, Duck Pond and Markle Pass, giant antidunes with characteristic

Antidunes in Camas Prairie (Missoula Flood)	
Initial lake level	1265 m
DEM source	USGS 3D ELEVATION
DEM resolution	1/3 arc-second
Grid size	10 m in Passes 68 m in Camas Prairie 300 m otherwise
Breach model	Instantaneous collapse
Gauge location	W4: 47° 32' 21" N 114° 34' 52.6" W
Wavelength ($\widehat{\Lambda}$)	100-150 m
Manning roughness	$\widehat{n} = 0.05$ s m$^{-1/3}$
Grain size	Pebble gravel with $\widehat{d} \approx 0.035$ m

Table 1: Summary of input data used in the formation study of antidunes in the Missoula Flood.

wavelengths of 82, 68, 92 and 86 m, and heights of 4.3, 2.3, 3.3 and 4.2 m, developed on slopes of 8, 4, 11.7 and 11.7 %, respectively. The transverse length of the antidune was limited by the bankfull width of the local channels where they grew, which are 200 m narrow. All of them are close to the outlet of the V-shaped valley pathways from the Little Bitterroot and Mission Basins to Camas Prairie (see also figure 8*a*). Lee argued that antidunes had been preserved there because flow ended abruptly when the water level dropped to the notch floor. We shall check if such a unique hydraulic regime developed according to the paleohydraulic reconstruction.

5.1.2. Required data

To estimate the probable maximum value of the flow velocity, Shields and Froude numbers in the Camas Prairie during the late stage of the largest Missoula flood, we followed the same modelling strategy as Bohorquez et al. (2016). The required input data is summarised in Table 1. As an initial condition, we set the Glacial Lake Missoula at an elevation of 1265 m (Pardee, 1942; Alho et al., 2010; Denlinger and O'Connell, 2010), see Fig. 8a. The extent of the computational domain included all the lakes upstream of the Flathead River (just before the confluence with the Clark Fork River up to the Mission Basin). Whereas the reach of interest for the paleohydraulic study lies at the Camas Prairie, the upstream lakes have been taken into account with the main aim of simulating the refilling of this basin through the Big Creek, Wills Creek, Markle and Duck Pond Pass. The ice-dam was assumed to collapse instantaneously (Denlinger and O'Connell, 2010) because antidunes developed at the end of the glacial-lake drainage, when the flow lost memory of the ice breach process. Simulated flooding areas, maps of water flow depth and two-dimensional velocity vectors were obtained by solving numerically the two-dimensional, unsteady shallow-water equations (1)-(2).

The paleohydraulic reconstruction required a thin spatial resolution (i.e. 10 m) to capture with accuracy the topographic flow control exerted at the outlet of the valley pathways. Hence, the computational mesh was created using a 1/3 arc-second DEM dated 2013 from the USGS 3D ELEVATION program (accessed at https://viewer.nationalmap.gov/basic). This is the highest resolution seamless DEM dataset for the U.S. A computational mesh with a cell size of about 10 m was created near the four inlet Passes where antidunes developed. Far from them, the computational grid was coarser with characteristic edge lengths of 68 m (300 m) inside (outside) of the Camas Prairie Basin. The computational mesh has 2.3 M cells and replicates real topography in the simulated region.

5.1.3. Results

Figure 8b depicts the map of the maximum value in time reached by the local Froude number during the draining and refilling of the Camas Prairie. The flow regime was subcritical in the Little Bitterroot Valley and the Mission Valley. Masses of water from the Little Bitterroot Basin passed over the ridges and refilled the Camas Prairie Basin while it drained through the Rainbow Lake Pass in the northwest part of the basin and the Perma Ridge in the south. The flow accelerated progressively and achieved a supercritical regime at the Wills Creek, Big Creek, Duck Pond and Markle Pass. The regime became subcritical as water entered the deepest region of the Camas Prairie. Over the extensions sculpted with antidunes (blue dashed area), the Froude number decreased to $\mathcal{F}r = 0.7$. Further downstream, due to the deep flow, we found $\mathcal{F}r < 0.5$. All these results are consistent with the developments of dunes and antidunes described in our linear stability theory (Section 4).

Figures 8c-d illustrate the high velocities and shallow depths simulated in the Wills Creek Pass and Markle Pass when lake level abruptly dropped to the notch floor at, approximately, $\widehat{t} = 24$ h. The speed was fastest than 15 m·s^{-1} and the local depth decreased below 60 m. The flow decelerated notably (i.e. < 2 m·s^{-1}) in the Camas Prairie Lake where flow was around 150-180 m deep. A mega-jet discharged from Little Bitterroot to a region where we presently find an enormous field (i.e. > 12 km in length) of giant dunes.

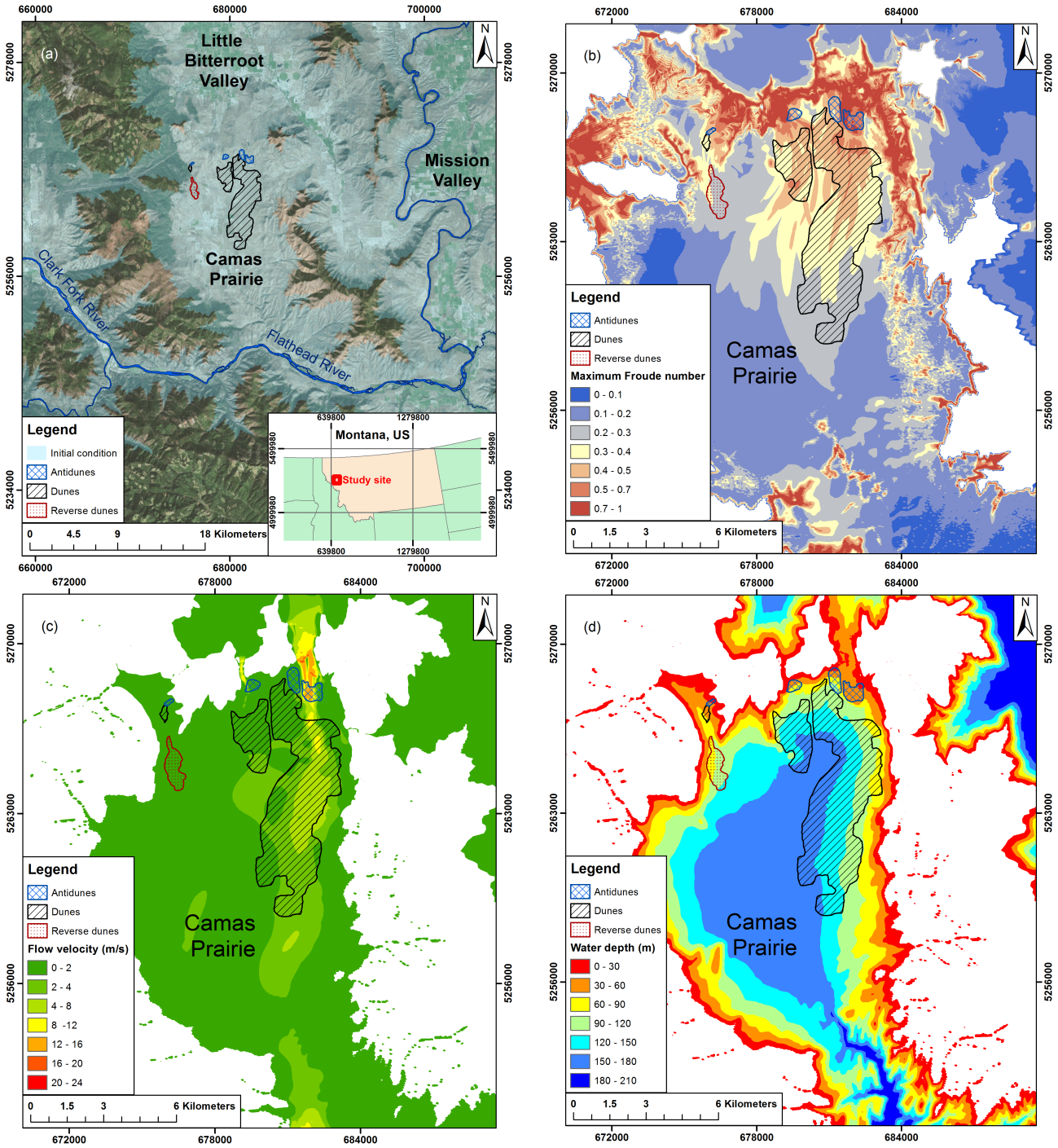

Fig. 8: (a) Zoom of the simulation area in the Camas Prairie and detail of the initial condition of the water elevation at 1265 m (Pardee, 1942), in geographic coordinate system UTM WGS84 Zone 11. (b) Maximum value of the Froude number achieved in the Camas Prairie Basin during the draining of the Missoula Lake. Snapshot of (c) velocity magnitude and (d) flow depth one day after the breach of the ice-dam, i.e. $\widehat{t} = 24$ h. See an animation of the instantaneous values of the flow depth, velocity magnitude, Shields parameter and Froude number over this area in Supplementary videos 2-5.

The velocity was nonuniform there because of the variable bathymetry and the dissipation of the jet throughout the lake expansion. As Pardee (1942) figured out, the unusual features at the Camas Prairie "appear to have been formed by large currents plunging over the north rim and continuing with decreasing velocity out into the basin".

The hydraulic regime that provoked the an-

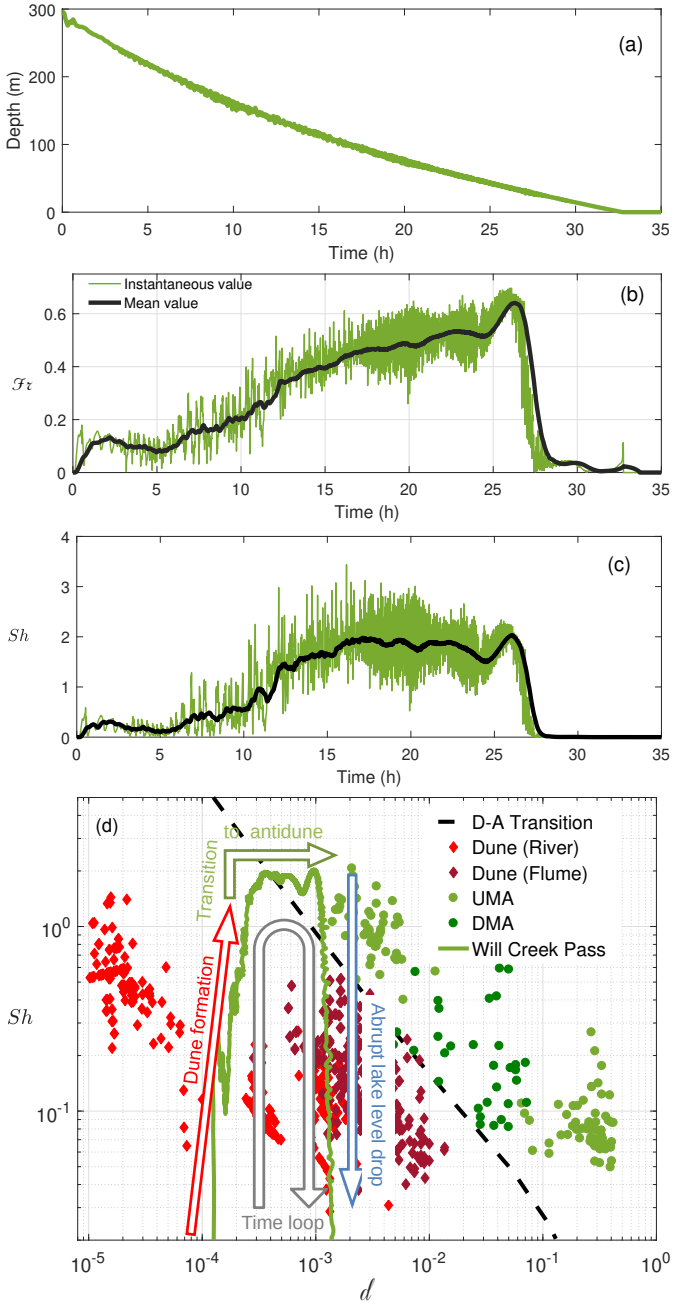

Fig. 9: Temporal evolution of (a) the flow depth, (b) Froude number and (c) Shields parameter over the antidunes in the Wills Creek Pass (see location in Fig. 1c). The green and black solid lines represent instantaneous and average magnitudes, respectively. (d) Comparison of the reconstructed nondimensional parameters and flume/river measurements in the parameter space $\{\ell, Sh\}$. The loop drawn by the simulated variables (green line) has been decomposed in three stages: early progressive inception of dune (red arrow); slow transition from dune to antidune (green arrow); sudden end when the lake level abruptly dropped to the notch floor ensuring the preservation of the antidune (blue arrow).

tidunes can be understood by visualising the temporal evolution of the Shields parameter, Froude number and flow depth on one of these bedforms at the Wills Creek Pass, see Fig. 9. The flow depth decreased monotonously over the antidune for, approximately, 32.6 h. The Froude number increased progressively to $\mathcal{F}r \approx 0.68$ for $\widehat{t} = 26$ h. The Shields parameter also rose during the first 15 hours but remained nearly constant ($Sh \approx 2$) in the period $15 \leq \widehat{t} \leq 26$ h. In a late stage ($26 \leq \widehat{t} \leq 28$ h), both the Froude and Shields numbers showed a sudden drop from $\mathcal{F}r = 0.68$ and $Sh = 2.3$ to $\mathcal{F}r \approx 0.05$ and $Sh \approx 0$ when flow depth was $\widehat{\eta} < 36$ m. A sharp decrease in velocity induced vanishing values of Sh and $\mathcal{F}r$. Therefore, our paleohydraulic reconstruction corroborates Lee's argument on the reason for the preservation of exceptional antidunes in the Camas Prairie Basin: "At Camas Prairie they may be preserved because of the unique paleohydraulic regime, in which current velocities did not decrease in a gradual manner, but dropped abruptly when lake level fell below the sublake notch".

As a matter of fact, the formation of antidunes can be justified using our stability diagram in the parameter space $\{\ell, Sh\}$ (Fig. 3c). To this end, we plotted in Fig. 9d the theoretical threshold for the dune-antidune transition (thick dashed line in black) and the curve $Sh(\ell)$ arising at the Wills Creek Pass (solid green line). For completeness, we included available experimental data from flume experiments and river measurements for dunes (red rhomboids) and antidunes (green circles). The first morphodynamic stage ($\widehat{t} < 10$ h) comprises the formation of giant dunes with $Sh < 0.5$ and $\ell < 2 \times 10^{-4}$. The corresponding Froude value satisfies $\mathcal{F}r < 0.2$. Then, the transition to antidune occurred in a second stage ($15 \leq \widehat{t} \leq 26$ h) characterised with the nondimensional parameters $3 \times 10^{-4} < \ell < 10^{-3}$ and $Sh \approx 2$. The maximum Froude number occurred at the late time ($\widehat{t} = 26$ h), with the set of nondimensional parameters $\{\mathcal{F}r = 0.68, \ell = 10^{-3}, k = 2.8, Sh = 2.3\}$ similar to those of (antidune) flume experiments over a sandy bed (Fig. 3). Lastly, the final stage was unusual because of the sudden decrease in $\mathcal{F}r$ and Sh with

Dunes in Kuray-Chuja Lakes (Altai Flood)		
Initial lake level		2100 m
DEM source		NASA SRTM v3.0
DEM resolution		1 arc-second
Grid size		50 m in Valleys 100 m in Kuray Basin 150 m in Chuja Basin
Breach model		Ice incision rate = 2.8 decametre/hour
Gauge	Kurai	50°11"4.86'N, 87°55'23.65"E
	Aktru	50°8'42.6"N, 87°50'11.1"E
	KamSugi	50°3'17.3"N, 88°28'39.5"E
$\widehat{\Lambda}$	Kurai	60-200 m
	Aktru	44-88 m
	KamSugi	59 m
Manning roughness		$\widehat{n} = 0.05$ s m$^{-1/3}$
Grain size		$\widehat{d} = 0.035$ m

Table 2: Summary of input data used in the formation study of dunes in the Altai Flood.

$10^{-3} < \ell < 1.4 \times 10^{-3}$, allowing the preservation of the antidune geological record.

5.2. Gravel dunes in the Kuray-Chuja Lakes

5.2.1. Study site

The catastrophic draining of the Kuray and Chuja Lakes in the Late Pleistocene provoked the formation of large fields of giant gravel dunes in the lake basin. The detailed description of the morphology and sedimentology of such large dunes can be found in earlier works (Carling, 1996; Carling et al., 2002; Herget, 2005). Among other soundness trains of dunes, we selected here for the analysis of the hydrodynamic processes those referred to as Kuray, Aktru and Kam Sugi. We have included the analysis of the Kuray dunes, see Fig. 1a, because it represents the most notable example of subaqueous gravel dunefields on Earth (Carling, 1999). There, the wavelength varies in the range of 60-200 m, the characteristic dune height is about 10-16 m, and the mean grain size is 35 mm.

5.2.2. Required data

The reconstruction of the dynamics of the drainage, following the method outlined in Section 2.1, has been detailed at length in a companion paper. Table 2 summarises the data used in the numerical simulations by Bohorquez, Jimenez-Ruiz and Carling (2019). We refer the reader to such a reference for further details on the numerical study. The growth of dunes in the Kuray and Chuja Lakes occurred in the early and middle stages of the failure of the ice dam. Hence, previous to the computation of the hydraulic variables in the lake basins, the ice-dam incision rate had to be determined. Once conducted, we evaluate the dimensionless parameters $\mathcal{F}\imath$, Sh and ℓ from the simulated flow depth and velocity in the lakes by setting set the characteristic value of grain size to $\widehat{d} = 0.035$ m as reported by Carling (1996) in the largest Kuray dune.

5.2.3. Results

We found that the Kuray dunefield developed due to the action of a mega eddy for 12 hours. The flow regime was two-dimensional and unsteady in the lake, while a nearly uniform flow occurred over the fields of bedforms. Characteristic flow depths and velocities achieved values of 157-537 m and 1.6-5 m·s^{-1} when $Sh > Sh_{cr}$. The corresponding Shields (Fig. 10a) and Froude (Fig. 10b) numbers were 0.03-0.14 and 0.04-0.1, respectively. Reconstructed values of nondimensional parameters were similar in rather different locations (e.g. Aktru and Kam Sugi) where other fields of large dunes formed. In Aktru, the Shields parameter achieved a maximum of 0.23, the Froude number remained around 0.1, and the fastest velocity was 5.5 m·s^{-1} with a flow depth of 310 m. The Shields number was above the threshold value of 0.03 during 12 h. In the Chuja lake, developments of giant dunes lasted for 40 h near Kam Sugi. The Shields parameter grew from 0.03 to 0.12 when the flow depth decreased from 330 to 50 m, and the Froude number was between 0.05 and 0.12. In the three studied locations, the simulated values

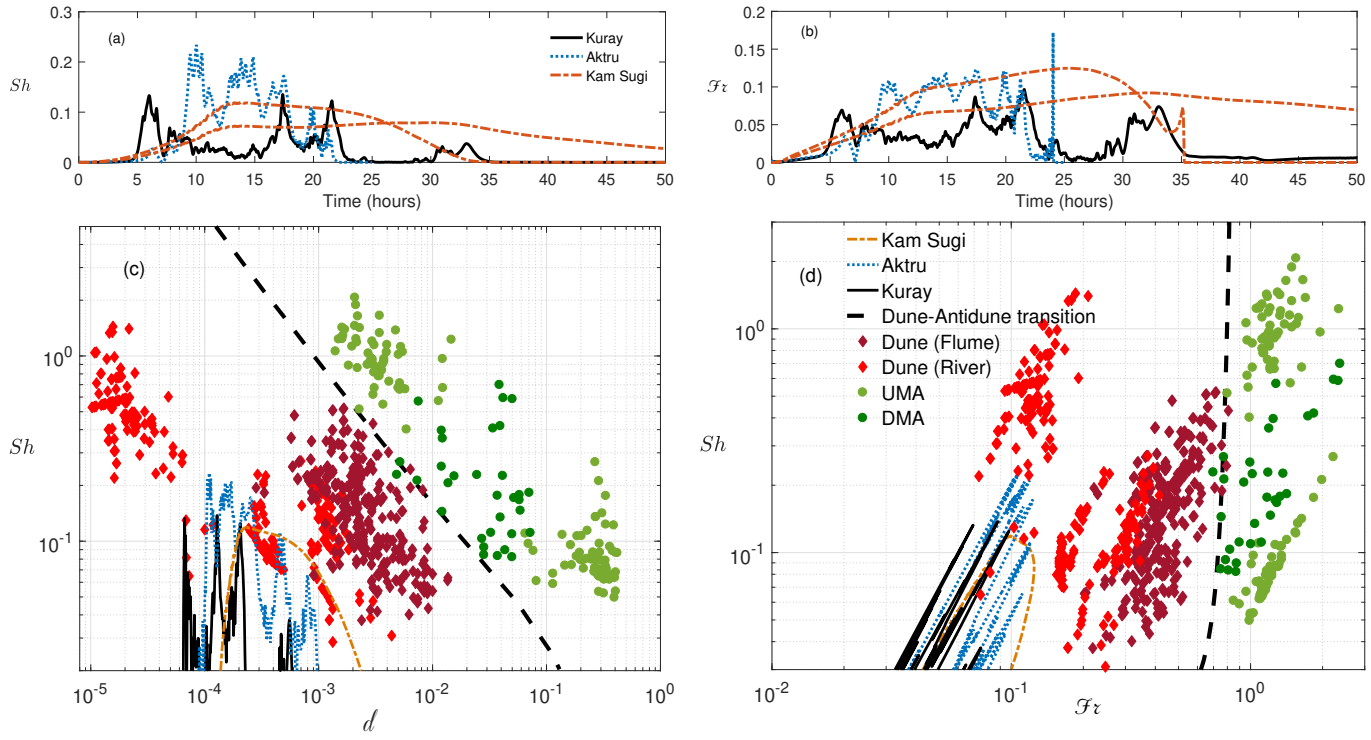

Fig. 10: Temporal evolution of the reconstructed (a) Shields and (b) Froude numbers in the large dunefields of Kuray, Aktru and Kam Sugi (Altai Mountains, Siberia). Comparison of the modelled nondimensional parameters and flume/river measurements in the parameter space (c) $\{\mathcal{d}, Sh\}$ and (d) $\{\mathcal{F}_\tau, Sh\}$.

of the Froude number are by the formation of the dune.

To discuss the similarities and differences between the conditions to form megaflood-scale dunes and lesser scales, we compare in Fig. 10 the nondimensional parameters $\mathcal{d}$ and Sh at the locations of interest (black: Kuray, blue: Aktru, orange: Kam Sugi) against well-controlled experiments (symbols). The theoretical curve of the dune-antidune transition (thick dashed line) is shown for completeness. The unsteady flow in Kuray, Aktru and Kam Sugi induces three curves, $Sh(\mathcal{d})$, whose shape depends on the spatial location, but they share some properties. At the onset, the roughness was of the order of $\mathcal{d} \sim O(10^{-4})$. As time proceeded, the lake depth decreased and, thus, the grain roughness relative to flow depth increased to $\mathcal{d} \sim O(10^{-3})$. The maximum value of the simulated Shields number (i.e. $Sh \sim 0.1 - 0.2$) and the corresponding grain roughness lie close to those parameters observed in sandy rivers (light red). Surprisingly, very large dunes in large sandy rivers exhibit a lower roughness (i.e. $10^{-5} \leq \mathcal{d} \leq 10^{-4}$) and a higher Shields parameter ($Sh > 0.2$). If we proceed with the comparison in the parameter space $\{\mathcal{F}_\tau, Sh\}$, see Fig 10d, it yields that the Froude number of the megaflood ($\mathcal{F}_\tau \approx 0.1$) is slightly lower than in sandy rivers ($\mathcal{F}_\tau \approx 0.2$). Alternatively, the Shields parameter during the Altai megaflood (i.e. $Sh < 0.2$) was lower than measured in large sandy rivers (i.e. $Sh > 0.2$) for the same Froude number ($\mathcal{F}_\tau \approx 0.1$).

Independently of the above results, the simulated hydraulic conditions over the Kuray and the Chuja dunefields yield values of Sh, $\mathcal{F}_\tau$ and $\mathcal{d}$ that lie in the theoretical region of dunes according to the proposed shallow-water formulation (i.e. below the dashed line in Figs. 10c-d or in the red area in Fig. 2). Subsequently, the proposed morphodynamic theory could be solved numerically in the future to simulate the growth and evolution of large dunes in megafloods on Earth.

6. Conclusions

The paleohydraulic reconstructions of the Altai megaflood and the largest Missoula flood reveal that giant antidunes and dunes developed with a characteristic lake depth and depth-averaged flow velocity in the wide range of values 50-500 m and 1.6-15 m·s^{-1}. Such high-speed flows, with characteristic Reynolds numbers of the order of $\mathcal{R}e \sim O(10^8 - 10^{10})$, support the dynamical simulation of the megaflood using a flow depth-averaged model as the Saint-Venant or shallow-water equations, i.e. the widest accepted technique in paleohydrology. To progress in the direct numerical simulation of the formation of megaflood-scale bedforms, we require a morphodynamic model based on the shallow-water equations able to predict the erodible bed instability that forms dunes and antidunes.

We have presented a simple depth-averaged morphodynamic theory that can predict the formation of such bedforms in water flows over erodible beds both at small scale flume experiments, large-scale rivers and megafloods. We have derived the formalism of the theory from an analytical, linear stability analysis in which the hydraulic resistance was lagged with respect to the mean flow velocity. The algebraic eigenvalue problem (20) determines the type of bedform, and its wavelength, as a function of the Froude number, $\mathcal{F}r$, and the nondimensional grain roughness, ℓ. Alternatively, instead of $\mathcal{F}r$, the Shields parameter, Sh, can be used. Furthermore, we worked a closed-form solution of the growth rate (25) and wave speed (26) of the bed disturbance using the quasi-steady assumption by Kennedy (1963). The approximate analytical solution converges to that of the full eigenvalue problem in the dune regime. The numerical resolution of the non-linear equations for a one-dimensional, supercritical flow showed, in a previous work, the model capability to capture the inception, growth and migration of bedforms (in particular, antidunes) in agreement with the linear stability results. Now, the revised formulation offers the new possibility of simulating bedforms in the subcritical regime (i.e. dunes) and large-scale geophysical flows as megafloods and very-large rivers.

Our three-dimensional bedform diagram takes into account not only the Froude (or Shields) number but also the grain roughness relative to flow depth, ℓ. We have shown the relevance of the grain roughness for the selection of the bedform as it depends on the spatial scale of the flow. The possible bedforms are: dune for $\ell \leq 10^{-3}$, antidune for $\ell > 10^{-2}$ and dune or antidune for $10^{-3} < \ell \leq 10^{-2}$ depending on $\mathcal{F}r$ or Sh. The current morphodynamic model correctly predicts the development of bedforms in large sandy rivers ($10^{-5} < \ell < 3 \times 10^{-3}$), flume experiments ($5 \times 10^{-4} < \ell < 5 \times 10^{-2}$) and gravel-bed rivers ($\ell > 5 \times 10^{-2}$). Also, the paleohydraulic reconstruction of giant antidunes and subaqueous gravel-dunes allowed us to set $\ell \sim O(10^{-3} - 10^{-4})$ for megafloods, which yields a flow depth $10^3 - 10^4$ times the grain size.

To conclude, there is a close analogy of the current morphodynamic model (1)-(8) and well-known non-equilibrium sediment transport equations, allowing to extend the capabilities of existing models by the inclusion of particle diffusivity and phase lag effects to simulate the formation of bedforms in a great variety of problems. In particular, the growth and evolution of large fields of bedforms under the flow conditions observed in the paleohydraulic reconstruction of mega-floods.

Acknowledgements

P.B. thanks Paul Carling for the invitation to write this article for the Earth-Science Reviews Special Volume "Megaflooding on Earth: A Global Perspective". This work was supported by the Spanish Ministry of Science, Innovation and Universities (MICINN/FEDER, UE) under Grant SEDRETO CGL2015-70736-R. P.C.P. and P.R.J. were supported by the European Social Fund and the University of Jaén. J.D.d.M.E. was supported by the PhD scholarship BES-2016-079117 (MICINN/FSE, UE) from the Spanish National Programme for the Promotion of Talent and its Employability (call 2016). Daniel Garcia-Castellanos is thanked for the image reproduced here as Fig. 1a.

March 27, 2019

Appendix A. Nondimensional closure laws of model parameters

Here, we follow Bohorquez and Ancey (2015) and rewrite the closure laws of the model variables $\{f,\, \nu,\, \alpha,\, \kappa_\gamma,\, \kappa_\eta,\, \gamma_{ss}\}$ in the nondimensional equations (14)-(17) as a function of the independent, control parameters $\{\ell,\, \mathcal{F}\mathfrak{r}\}$. The remaining model parameter β takes a constant value.

To evaluate the friction factor, f, we set the bed roughness to $4\,d$ (d is the mean grain diameter), and we assume a channel width much larger than the flow depth $\widehat{\eta}_0$ with hydraulic diameter $\widehat{D}_h = 4\,\widehat{\eta}_0$. In doing so, f is assumed to be a nonlinear function of the relative grain roughness and is evaluated from the empirical Colebrook equation in fully developed turbulent flow and rough regime

$$\frac{1}{\sqrt{f}} = -2\,\log\left(\frac{\ell}{3.71\,\eta}\right)\,. \tag{A.1}$$

The correctness of Colebrook's empirical approach to model the bottom shear stress has been shown in numerous comparisons with flume measurements. Indeed, most of the experimental studies summarised in Fig. 3, which accounts for 500 experimental runs, have verified the applicability of the Darcy-Weisbach hydraulic resistance law even in the presence of dunes, antidunes and roll waves.

A rough estimation of the dimensionless eddy viscosity is given by $\nu = \nu_t\sqrt{f/8}$ with the constant parameter $\nu_t \sim O(1)$. The parametric dependence of the particle diffusivity α on the flow variables remains unexplored to our knowledge and, because of this, we evaluate it assuming a constant value of the turbulent Schmidt number, $Sc = \nu/\alpha = 0.5$. We set $\nu_t = 1$ for the sake of simplicity. Also, we fix the sediment-to-water velocity ratio at $\beta = 1$.

Using the scaling laws by Lajeunesse, Malverti and Charru for the dimensional deposition rate, $\widehat{\kappa}$, and the equilibrium particle activity, $\widehat{\gamma}_0$ (see Charru et al., 2013; Bohorquez and Ancey, 2015, and references therein), we arrive at the expressions $\kappa_\eta = 0.1\,(s-1)^{1/2}/(\mathcal{F}\mathfrak{r}\,\ell^{1/2})$ and $\kappa_\gamma/\kappa_\eta \approx 14\,\ell\,(Sh^\varphi - Sh_{cr})$ for $\zeta_b = 0.4$ and spherical particles. The Shields parameter, Sh^φ, represents the dimensionless shear stress,

$$Sh^\varphi = \frac{f\,\widehat{u}_0^2\,u^{\varphi 2}}{8\,(s-1)\,\widehat{g}\,\widehat{\eta}_0\,\ell} = \frac{f\,\mathcal{F}\mathfrak{r}^2}{8\,(s-1)\,\ell}\,u^{\varphi 2}\,. \tag{A.2}$$

The lowest threshold value of incipient motion for sand and gravel in hydraulically rough turbulent flow is typically $Sh_{cr} = 0.02$ (Julien, 2010).

Lastly, the saturated particle activity, referred to as γ_{ss} in (16)–(17), can be evaluated from any suitable empirical relationship for the sediment discharge and lags a distance φ/k behind the local velocity at the perturbed bed due to its dependence on the dimensionless shear stress (Kennedy, 1963, 1969). Taking into account this point, and using the same closure law as Bohorquez and Ancey (2015), we set $\gamma_{ss}^\varphi = \gamma_{ss}(Sh^\varphi)$ with

$$\gamma_{ss}(Sh) = \begin{cases} \frac{Sh - Sh_{cr}}{Sh_0 - Sh_{cr}} & \text{if} \quad Sh \geq Sh_{cr}\,, \\ 0 & \text{if} \quad Sh < Sh_{cr}\,. \end{cases} \tag{A.3}$$

The Shields number of the base flow, Sh_0, must be greater than Sh_{cr} to erode sediment (i.e. $\gamma_{ss} > 0$). Next, the base-flow Shields number is obtained by setting $u^\varphi = 1$ into (A.2),

$$Sh_0 = \frac{S}{(s-1)\,\ell} \quad \text{with} \quad S = \frac{f_0}{8}\,\mathcal{F}\mathfrak{r}^2\,. \tag{A.4}$$

Note that Sh_0 and S can be evaluated using (A.1) from the two independent parameters that characterise the base flow, namely ℓ and $\mathcal{F}\mathfrak{r}$. Sh_0 also affects the stability of the base flow through the linear response of γ_{ss} to a small change of the flow velocity with respect to the base flow (denoted by γ'_{ss} in Sections 4.2 and 4.3):

$$\begin{aligned} \gamma'_{ss} &= \left.\frac{\mathrm{d}\gamma_{ss}}{\mathrm{d}u}\right|_{\substack{u=1\\ \eta=1}} = \left.\frac{\mathrm{d}\gamma_{ss}}{\mathrm{d}Sh}\right|_{Sh=Sh_0} \left.\frac{\mathrm{d}Sh}{\mathrm{d}u}\right|_{u=1} \\ &= \frac{2\,Sh_0}{Sh_0 - Sh_{cr}}\,. \end{aligned} \tag{A.5}$$

Appendix B. Derivation of the eigenvalue problem

We consider the linear stability analysis of a steady, uniform flow down an erodible bed inclined at a constant slope, S, with respect to the

horizontal. The base-flow solution to the Saint–Venant–Exner equations (14)–(16) is straightforward: $\eta = u = 1$ and $z = -S\,x$ with $\gamma = 1$ in (17).

Substituting the expansion $(\eta, u, \gamma, z) = (1, 1, 1, -x\,S) + \epsilon\,(\eta_\epsilon, u_\epsilon, \gamma_\epsilon, z_\epsilon)$ into (14)–(17), expanding f and γ_{ss} in a Taylor series about the base flow, and retaining only the terms of the order $O(\epsilon)$, we end up with the linear perturbation equations:

$$\frac{\partial \eta_\epsilon}{\partial t} + \frac{\partial \eta_\epsilon}{\partial x} + \frac{\partial u_\epsilon}{\partial x} = 0\,, \tag{B.1}$$

$$\mathcal{F}\mathfrak{r}^2 \left(\frac{\partial u_\epsilon}{\partial t} + \frac{\partial u_\epsilon}{\partial x} - \nu \frac{\partial^2 u_\epsilon}{\partial x^2} \right) + \frac{\partial \eta_\epsilon}{\partial x} = -\frac{\partial z_\epsilon}{\partial x} + S\,(\eta_\epsilon - 2\,u_\epsilon^\varphi)\,, \tag{B.2}$$

$$\frac{\partial z_\epsilon}{\partial t} = \kappa_\gamma\,(\gamma_\epsilon - u_\epsilon^\varphi\,\gamma'_{ss})\,, \tag{B.3}$$

$$\frac{\partial \gamma_\epsilon}{\partial t} + \beta \left(\frac{\partial u_\epsilon}{\partial x} + \frac{\partial \gamma_\epsilon}{\partial x} \right) - \alpha \frac{\partial^2 \gamma_\epsilon}{\partial x^2} = \kappa_\eta\,(u_\epsilon^\varphi\,\gamma'_{ss} - \gamma_\epsilon)\,. \tag{B.4}$$

The term f' was neglected in (B.2)–(B.4) due to $\delta \ll 1$. In (B.3)-(B.4), the lagged velocity is evaluated as $u_\epsilon^\varphi \to u_\epsilon(x + \varphi/k, t)$.

The solution to the linear perturbation equations (B.1)–(B.4) in the temporal stability analysis can be written as $(\eta_\epsilon, u_\epsilon, \gamma_\epsilon, z_\epsilon) = (H_\epsilon, V_\epsilon, G_\epsilon, Z_\epsilon)^T \exp[\mathrm{i}(k\,x - \omega\,t)]$ where the real wavenumber is denoted by k and the complex frequency by $\omega = \omega_r + \mathrm{i}\,\omega_i$ (Schmid and Henningson, 2001). The normal-mode analysis with lag proceeds as usual except that we must set $u_\epsilon^\varphi = u_\epsilon(x,t)\exp(\mathrm{i}\,\varphi)$ in (B.3)-(B.4). The solutions to the linear perturbation equations (B.1) and (B.3) establish a relation between the eigenvector components H_ϵ and Z_ϵ, respectively, as a function of G_ϵ and V_ϵ, allowing for the reduction of the eigenproblem by means of

$$H_\epsilon = \frac{k}{\omega - k}\,V_\epsilon\,, \tag{B.5}$$

$$Z_\epsilon = \frac{\mathrm{i}\,\kappa_\gamma}{\omega}\,G_\epsilon - \frac{\mathrm{i}\,\gamma'_{ss}\,\kappa_\gamma}{\omega}\,V_\epsilon\,\exp(\mathrm{i}\,\varphi)\,. \tag{B.6}$$

Using (B.5)–(B.6), the complex eigenvalue, ω, and eigenvector, $\mathbf{T} \equiv (G_\epsilon, V_\epsilon)^T$, were obtained from the generalised eigenproblem, $\mathbf{A}\cdot\mathbf{T} = 0$, where the stability matrix is given by (20).

Appendix C. Derivation of the bedform growth rate and wave speed

The continuity equation (21) can be readily integrated, subject to the base flow condition $A_0 = 1 - U$ for $u = 1$ and $\eta = 1$, to show that the depth-averaged velocity is

$$u = \frac{A_0}{\eta} + U = \frac{1-U}{\eta} + U\,. \tag{C.1}$$

Substitution of (C.1) into (22) yields

$$\frac{\partial}{\partial \xi}\left[\mathcal{F}\mathfrak{r}^2 \frac{A_0}{\eta}\left(A_0 + \nu \frac{\partial \eta}{\partial \xi} \right) + \frac{\eta^2}{2} \right] = -\eta\,\frac{\partial z}{\partial \xi} - \mathcal{F}\mathfrak{r}^2 \frac{f}{8}\left(U + \frac{A_0}{\eta} \right)^2\,. \tag{C.2}$$

Following Kennedy, we then introduce the asymptotic sequences $(\eta,\ u,\ \gamma,\ z) = [1,\ 1,\ 1,\ -z_0(\xi,\tau)] + \varepsilon(\tau)\ [\eta_\varepsilon(\xi),\ u_\varepsilon(\xi),\ \gamma_\varepsilon(\xi),\ z_\varepsilon(\xi)]$ with $z_0 = -(U\,\tau + \xi)\,S$ and $z_\varepsilon = \exp(\mathrm{i}\,k\,\xi)$. Substituting it into (C.2), we end up with a second-order ordinary differential equation (ODE) for η_ε at the linear order,

$$\frac{\mathrm{d}^2 \eta_\varepsilon}{\mathrm{d}\xi^2} + \frac{1 - \mathcal{F}\mathfrak{r}^2\,(1-U)^2}{\mathcal{F}\mathfrak{r}^2\,\nu\,(1-U)}\,\frac{\mathrm{d}\eta_\varepsilon}{\mathrm{d}\xi} + \frac{S\,(2\,U-3)}{\mathcal{F}\mathfrak{r}^2\,\nu\,(1-U)}\,\eta_\varepsilon = -\frac{\mathrm{i}\,k\,\exp(\mathrm{i}\,k\,\xi)}{\mathcal{F}\mathfrak{r}^2\,\nu\,(1-U)}\,, \tag{C.3}$$

whose solution is given by $\eta_\varepsilon = H_\varepsilon\,\exp(\mathrm{i}\,k\,\xi)$ and

$$\begin{aligned} H_\varepsilon &= (H_r + \mathrm{i}\,H_i)^{-1}\,, \\ H_r &= \mathcal{F}\mathfrak{r}^2\,(U-1)^2 - 1\,, \\ H_i &= \mathcal{F}\mathfrak{r}^2\,k\,\nu\,(U-1) + S\,k^{-1}\,(2\,U-3)\,. \end{aligned} \tag{C.4}$$

Next, the velocity perturbation is evaluated from the algebraic relation (C.1) as $u_\varepsilon = V_\varepsilon\,\exp(\mathrm{i}\,k\,\xi)$, where $V_\varepsilon = (U-1)\,H_\varepsilon$.

Subsequently, (24) leads to the following ODE for γ_ε,

$$-\alpha\frac{\mathrm{d}^2\gamma_\varepsilon}{\mathrm{d}\xi^2} + (\beta - U)\,\frac{\mathrm{d}\gamma_\varepsilon}{\mathrm{d}\xi} + \kappa_\eta\,\gamma_\varepsilon = \kappa_\eta\,\gamma'_{ss}\,u_\varepsilon^\varphi - \beta\,\frac{\mathrm{d}u_\varepsilon}{\mathrm{d}\xi}\,. \tag{C.5}$$

The solution to (C.5) can be expressed in compact form as

$$\gamma_\varepsilon = G_\varepsilon \exp(\mathrm{i}\, k\, \xi) + G_{\varepsilon\varphi} \exp[\mathrm{i}\, (k\, \xi + \varphi)]\,, \quad \text{(C.6)}$$

$$G_\varepsilon = \frac{k\,(1-U)\;\beta}{(H_i - \mathrm{i}\, H_r)\,[\alpha\, k^2 - \mathrm{i}k\,(U-\beta) + \kappa_\eta]}\,, \quad \text{(C.7)}$$

$$G_{\varepsilon\varphi} = \frac{(1-U)\,\mathrm{i}\,\gamma'_{ss}\,\kappa_\eta}{(H_i - \mathrm{i}\, H_r)\,[\alpha\, k^2 - \mathrm{i}k\,(U-\beta) + \kappa_\eta]}\,. \quad \text{(C.8)}$$

Finally, using the same procedure in the equation of the bed-stream interface (23), we worked out a closed-form solution to the growth rate and wave speed of the bed disturbance. Linearising (23) in the perturbation amplitude, ε, leads to

$$z_\varepsilon \frac{\mathrm{d}\varepsilon}{\mathrm{d}\tau} - \varepsilon\, U\, \frac{\mathrm{d}z_\varepsilon}{\mathrm{d}\xi} = \varepsilon\, \kappa_\gamma\, (\gamma_\varepsilon - \gamma'_{ss}\, u^\varphi_\varepsilon)\;, \quad \text{(C.9)}$$

which can be attacked analytically. Substitution of the previous solutions for z_ε, γ_ε and u_ε into (C.9) generates the complex equation

$$\frac{\mathrm{d}\varepsilon}{\mathrm{d}\tau} - \varepsilon\, U\, \mathrm{i}\, k = \varepsilon\, \kappa_\gamma\, [G_\varepsilon + (G_{\varepsilon\varphi} - V_\varepsilon\, \gamma'_{ss}) \exp(\mathrm{i}\, \varphi)]\;. \quad \text{(C.10)}$$

Using the superscripts $\Re$ and $\Im$ to denote the real and imaginary parts of an algebraic expression, and taking the real part of (C.10), allow us to obtain the closed-form solution of the growth rate

$$\lambda \equiv \frac{1}{\varepsilon}\frac{\mathrm{d}\varepsilon}{\mathrm{d}\tau} = \kappa_\gamma \left[G^\Re_\varepsilon + \cos(\varphi)\left(G^\Re_{\varepsilon\varphi} - V^\Re_\varepsilon \gamma'_{ss}\right)\right] - \kappa_\gamma \left[\sin(\varphi)\left(G^\Im_{\varepsilon\varphi} - V^\Im_\varepsilon \gamma'_{ss}\right)\right]\;. \quad \text{(C.11)}$$

Separating the imaginary part of (C.10) then furnishes an implicit equation for U:

$$U = -\frac{\kappa_\gamma}{k}\left[G^\Im_\varepsilon + \cos(\varphi)\left(G^\Im_{\varepsilon\varphi} - V^\Im_\varepsilon \gamma'_{ss}\right)\right] - \frac{\kappa_\gamma}{k}\sin(\varphi)\left(G^\Re_{\varepsilon\varphi} - V^\Re_\varepsilon \gamma'_{ss}\right)\;. \quad \text{(C.12)}$$

The algebraic expressions of the growth rate, λ, and wave speed, U, of the bedform are obtained by substituting the real and imaginary parts of (C.7)-(C.8) into (C.11) and (C.12). A little algebra generates the lengthy algebraic expressions (25)-(30).

References

Abril-Hernández, J., Periáñez, R., O'Connor, J., Garcia-Castellanos, D., 2018. Computational Fluid Dynamics simulations of the Late Pleistocene Lake Bonneville Flood. Journal of Hydrology 561, 1–15. doi:10.1016/j.jhydrol.2018.03.065.

Ackers, P., White, M.M., 1973. Sediment transport: new approach and analysis. J. Hydraul. Div. ASCE 99, 2041–2060.

Alho, P., Baker, V., Smith, L., 2010. Paleohydraulic reconstruction of the largest Glacial Lake Missoula draining(s). Quaternary Science Reviews 29, 3067–3078. doi:10.1016/j.quascirev.2010.07.015.

Ancey, C., 2010. Stochastic modeling in sediment dynamics: Exner equation for planar bed incipient bed load transport conditions. J. Geophys. Res. 115, F00A11.

Ancey, C., Bohorquez, P., Heyman, J., 2015. Stochastic interpretation of the advection-diffusion equation and its relevance to bed load transport. J. Geophys. Res. Earth Surf. 120, 2529–2551. doi:10.1002/2014JF003421.

Ancey, C., Heyman, J., 2014. A microstructural approach to bed load transport: mean behaviour and fluctuations of particle transport rates. J. Fluid Mech. 744, 129–168. doi:10.1017/jfm.2014.74.

Anderson, L., 1953. The characteristics of sediment waves formed by flow in open channels, in: Proc. Third Mid-Western Conf. on Fluid Mech., University of Minnesota. pp. 379–395.

Andreotti, B., Claudin, P., Devauchelle, O., Durán, O., Fourrière, A., 2012. Bedforms in a turbulent stream: ripples, chevrons and antidunes. J. Fluid Mech. 690, 94–128. doi:10.1017/jfm.2011.386.

Baines, P., Whitehead, J., 2003. On multiple states in single-layer flows. Phys. Fluids 15, 298–307. doi:10.1063/1.1531178.

Baker, V., 2013. Global late quaternary fluvial paleohydrology with special emphasis on paleofloods and megafloods, in: Shroder, J., Wohl, E.E. (Eds.), Treatise on geomorphology, Vol. 9, Fluvial geomorphology, San Diego, California, Academic Press. p. 511–527.

Baker, V., Benito, G., Rudoy, A., 1993. Paleohydrology of late pleistocene superflooding, Altay mountains, Siberia. Science 259, 348–350. doi:10.1126/science.259.5093.348.

Baker, V.R., 1973. Paleohydrology and sedimentology of lake Missoula flooding in Eastern Washington. Special Paper of the Geological Society of America 144, 1–73. doi:10.1130/SPE144-p1.

Baker, V.R., 1987. Paleoflood hydrology and extraordinary flood events. J. Hydrol. 96, 79–99.

Baker, V.R., 2009. Overview of megaflooding: Earth and Mars, in: Burr, D. M., Carling, P. A., Baker, V. R. (Eds.), Megaflooding on Earth and Mars, Cambridge University Press, Cambridge. pp. 1—12. doi:10.1017/CBO9780511635632.001.

Ballio, F., Pokrajac, D., Radice, A., Hosseini-Sadabadi,

S.A., 2018. Lagrangian and Eulerian description of bed load transport. Journal of Geophysical Research: Earth Surface 123, 384–408. doi:10.1002/2016JF004087.

Balmforth, N.J., Provenzale, A., 2001. Patterns of dirt, in: Balmforth, N.J., Provenzale, A. (Eds.), Geomorphological Fluid Mechanics. Springer, pp. 369–393. doi:10.1007/3-540-45670-8_15.

Balmforth, N.J., Vakil, A., 2012. Cyclic steps and roll waves in shallow water flow over an erodible bed. J. Fluid Mech. 695, 35–62. doi:10.1017/jfm.2011.555.

Berger, M., George, D., LeVeque, R., Mandli, K., 2011. The GeoClaw software for depth-averaged flows with adaptive refinement. Advances in Water Resources 34, 1195–1206. doi:10.1016/j.advwatres.2011.02.016.

Bohorquez, P., 2016. Paleohydraulic reconstruction of modern large floods at subcritical speed in a confined valley: Proof of concept. Water 8, 567. doi:10.3390/w8120567.

Bohorquez, P., Ancey, C., 2015. Stochastic-deterministic modeling of bed load transport in shallow water flow over erodible slope: linear stability analysis and numerical simulation. Adv. Water Resour. 83, 36–54. doi:10.1016/j.advwatres.2015.05.016.

Bohorquez, P., Ancey, C., 2016. Particle diffusion in non-equilibrium bedload transport simulations. Appl. Math. Model. 40, 7474–7492. doi:10.1016/j.apm.2016.03.044.

Bohorquez, P., Carling, P., Herget, J., 2016. Dynamic simulation of catastrophic late Pleistocene glacial-lake drainage, Altai Mountains, central Asia. International Geology Review 58, 1795–1817. doi:10.1080/00206814.2015.1046956.

Bohorquez, P., Darby, S., 2008. The use of one- and two-dimensional hydraulic modelling to reconstruct a glacial outburst flood in a steep Alpine valley. Journal of Hydrology 361, 240–261. doi:10.1016/j.jhydrol.2008.07.043.

Bohorquez, P., Jimenez-Ruiz, P.J., Carling, P.A., 2019. Revisiting the dynamics of catastrophic late Pleistocene glacial-lake drainage, Altai Mountains, central Asia. Earth Sci Rev. , (submitted).

Bohorquez, P., del Moral-Erencia, J., 2017. 100 years of competition between reduction in channel capacity and streamflow during floods in the Guadalquivir River (Southern Spain). Remote Sensing 9. doi:10.3390/rs9070727.

Bose, S., Dey, S., 2009. Reynolds averaged theory of turbulent shear flows over undulating beds and formation of sand waves. Phys. Rev. E 80. doi:10.1103/PhysRevE.80.036304.

Bradley, R.W., Venditti, J.G., 2017. Reevaluating dune scaling relations. Earth-Sci. Rev. 165, 356–376. doi:10.1016/j.earscirev.2016.11.004.

Brock, R.R., 1969. Development of roll-wave trains in open channels. J. Hydraul. Div. 95, 1401–1427.

Camporeale, C., Ridolfi, L., 2011. Modal versus nonmodal linear stability analysis of river dunes. Phys. Fluids 23, 104102. doi:10.1063/1.3644673.

Cao, Z., Li, Z., Pender, G., Hu, P., 2010. Non-capacity or capacity model for fluvial sediment transport. Water Manage. 165, 193–211.

Cao, Z., Pender, G., Wallis, S., Carling, P.A., 2004. Computational dam-break hydraulics over erodible bed. J. Hydraul. Eng. 130, 689–703.

Cao, Z., Xia, C., Pender, G., Liu, Q., 2017. Shallow water hydro-sediment-morphodynamic equations for fluvial processes. Journal of Hydraulic Engineering 143. doi:10.1061/(ASCE)HY.1943-7900.0001281.

Carling, .A., Leclair, S.F., 2018. Alluvial stratification styles in a large, flash-flood influenced dryland river: The luni river, Thar Desert, north-west India. Sedimentology doi:10.1111/sed.12487.

Carling, P., 1996. Morphology, sedimentology and palaeohydraulic significance of large gravel dunes, Altai Mountains, Siberia. Sedimentology 43, 647–664. doi:10.1111/j.1365-3091.1996.tb02184.x.

Carling, P., 1999. Subaqueous gravel dunes. J. Sediment. Res. 69, 534. doi:10.2110/jsr.69.534.

Carling, P., 2013. Freshwater megaflood sedimentation: What can we learn about generic processes? Earth-Science Reviews 125, 87–113. doi:10.1016/j.earscirev.2013.06.002.

Carling, P., Kirkbride, A., Parnachov, S., Borodavko, P., Berger, G., 2002. Late Quaternary catastrophic flooding in the Altai Mountains of south-central Siberia: A synoptic overview and an introduction to flood deposit sedimentology. International Association of Sedimentologists Special Publications , 17–35.

Carling, P., Villanueva, I., Herget, J., Wright, N., Borodavko, P., Morvan, H., 2010. Unsteady 1d and 2d hydraulic models with ice dam break for Quaternary megaflood, Altai Mountains, southern Siberia. Global and Planetary Change 70, 24–34. doi:10.1016/j.gloplacha.2009.11.005.

Carling, P.A., Bristow, C.S., Litvinov, A.S., 2016. Ground-penetrating radar stratigraphy and dynamics of megaflood gravel dunes. J. Geol. Soc. 173, 550–559. doi:10.1144/jgs2015-119.

Carling, P.A., Burr, D.M., Johnsen, T.F., Brennand, T.A., 2009a. A review of open-channel megaflood depositional landforms on Earth and Mars, in: Burr, D.M., Carling, P.A., Baker, V.R. (Eds.), Megaflooding on Earth and Mars, Cambridge University Press. pp. 33—49. doi:10.1017/CBO9780511635632.003.

Carling, P.A., Herget, J., Lanz, J.K., Richardson, K., Pacifici, A., 2009b. Channel-scale erosional bedforms in bedrock and in loose granular material: Character, processes and implications, in: Burr, D. M., Carling, P. A., Baker, V. R. (Eds.), Megaflooding on Earth and Mars, Cambridge University Press, Cambridge. pp. 13–32. doi:10.1017/CBO9780511635632.002.

Carling, P.A., Shvidchenko, A.B., 2002. A consideration of

the dune:antidune transition in fine gravel. Sedimentology 49, 1269–1282. doi:10.1046/j.1365-3091.2002.00496.x.

Carrivick, J.L., 2006. Application of 2D hydrodynamic modelling to high–magnitude outburst floods: An example from Kverkfjöll, Iceland. J. Hydrol. 321, 187–199.

Charru, F., 2006. Selection of the ripple length on a granular bed sheared by a liquid flow. Phys. Fluids 18, 121508.

Charru, F., Andreotti, B., Claudin, P., 2013. Sand ripples and dunes. Annu. Rev. Fluid Mech. 45, 469–493. doi:10.1146/annurev-fluid-011212-140806.

Cheng, N.S., 2016. Comparison of sediment-pickup rates over plane bed and dunes. J. Hydraul. Eng. 142, 04016057. doi:10.1061/(ASCE)HY.1943-7900.0001204.

Deigaard, R., 2006. Breaking antidunes: Cyclic behavior due to hysteresis. J. Hydraul. Eng. 132, 620–623. doi:10.1061/(ASCE)0733-9429(2006)132:6(620).

Denlinger, R., O'Connell, D., 2010. Simulations of cataclysmic outburst floods from Pleistocene glacial lake Missoula. Bulletin of the Geological Society of America 122, 678–689. doi:10.1130/B26454.1.

Dey, S., 2014. Fluvial Hydrodynamics: Hydrodynamic and Sediment Transport Phenomena. Springer. doi:10.1007/978-3-642-19062-9.

Di Cristo, C., Iervolino, M., Vacca, A., 2006. Linear stability analysis of a 1-D model with dynamical description of bed-load transport. J. Hydraul. Res. 44, 480–487.

van Duin, O., Hulscher, S., Ribberink, J., Dohmen-Janssen, C., 2017. Modeling of spatial lag in bed-load transport processes and its effect on dune morphology. Journal of Hydraulic Engineering 143. doi:10.1061/(ASCE)HY.1943-7900.0001254.

El Kadi Abderrezzak, K., Paquier, A., 2009. One-dimensional numerical modeling of sediment transport and bed deformation in open channels. Water Resour. Res. 45, W05404.

Feldman, A.D., 1981. HEC models for water resources system system simulation: theory and experience. Adv. Hydrosci. 12, 297–423.

Fernandez Luque, R., van Beek, R., 1976. Erosion and transport of bed-load sediment 14, 127–144.

Fourrière, A., Claudin, P., Andreotti, B., 2010. Bedforms in a turbulent stream: Formation of ripples by primary linear instability and of dunes by nonlinear pattern coarsening. J. Fluid Mech. 649, 287–328. doi:10.1017/S0022112009993466.

Frederick, K., Hanratty, T., 1988. Velocity measurements for a turbulent nonseparated flow over solid waves. Exp Fluids 6, 477–486. doi:10.1007/BF00196509.

Froude, M., Alexander, J., Barclay, J., Cole, P., 2017. Interpreting flash flood palaeoflow parameters from antidunes and gravel lenses: An example from Montserrat, West Indies. Sedimentology 64, 1817–1845. doi:10.1111/sed.12375.

Furbish, D.J., Ball, A.E., Schmeeckle, M.W., 2012a. A probabilistic description of the bed load sediment flux: 4. Fickian diffusion at low transport rates. J. Geophys. Res. 117, F03034.

Furbish, D.J., Haff, P.K., Roseberry, J.C., Schmeeckle, M.W., 2012b. A probabilistic description of the bed load sediment flux: 1. Theory. J. Geophys. Res. 117, F03031.

García, M.H., 2007. Sediment transport and morphodynamics, in: García, M.H. (Ed.), Sedimentation Engineering. American Society of Civil Engineers, Reston. volume ASCE Manuals and Reports on Engineering Practice 110, pp. 21–164.

George, D., 2011. Adaptive finite volume methods with well-balanced Riemann solvers for modeling floods in rugged terrain: Application to the Malpasset dam-break flood (France, 1959). International Journal for Numerical Methods in Fluids 66, 1000–1018. doi:10.1002/fld.2298.

Gradowczyk, M.H., 1968. Wave propagation and boundary instability in erodible-bed channels. J. Fluid Mech. 33, 93–112. doi:10.1017/S0022112068002387.

Grant, G., 1994. Hydraulics and sediment transport dynamics controlling step-pool formation in high gradient streams: A flume experiment, in: Ergenzinger, P., Schmidt, K.H. (Eds.), Dynamics and Geomorphology of Mountain Rivers, Springer Berlin Heidelberg, Berlin, Heidelberg. pp. 241–250. doi:10.1007/BFb0117843.

Greco, M., Iervolino, M., Vacca, A., 2017. Analysis of bedform instability with 1-D two-phase morphodynamical models. Adv. Water Resour. doi:10.1016/j.advwatres.2017.07.002.

Guan, M., Wright, N., Sleigh, P., Carrivick, J., 2015. Assessment of hydro-morphodynamic modelling and geomorphological impacts of a sediment-charged jökulhlaup, at Sólheimajökull, Iceland. Journal of Hydrology 530, 336–349. doi:10.1016/j.jhydrol.2015.09.062.

Herget, J., 2005. Reconstruction of Pleistocene ice-dammed lake outburst floods in the Altai Mountains, Siberia. Special Paper of the Geological Society of America 386, 1–118. doi:10.1130/0-8137-2386-8.1.

Herget, J., Roggenkamp, T., Krell, M., 2014. Estimation of peak discharges of historical floods. Hydrol. Earth Syst. Sci. 18, 4029–4037.

Heyman, J., Bohorquez, P., Ancey, C., 2016. Entrainment, motion and deposition of coarse particles transported by water over a sloping mobile bed. J. Geophys. Res. Earth Surf. 121, 1931–1952. doi:doi:10.1002/2015JF003672.

Huang, W., Cao, Z., Pender, G., Liu, Q., Carling, P., 2015. Coupled flood and sediment transport modelling with adaptive mesh refinement. Science China Technological Sciences 58, 1425–1438. doi:10.1007/s11431-015-5880-6.

Huang, W., Cao, Z.X., Carling, P., Pender, G., 2014. Coupled 2D hydrodynamic and sediment transport modeling of megaflood due to glacier dam-break in Altai

Mountains, Southern Siberia. Journal of Mountain Science 11, 1442–1453. doi:10.1007/s11629-014-3032-2.

Julien, P.Y., 2010. Erosion and Sedimentation. Cambridge University Press, Cambridge.

Julien, P.Y., Raslan, Y., 1998. Upper-regime plane bed. J. Hydraul. Eng. 124, 1086–1096. doi:10.1061/(ASCE)0733-9429(1998)124:11(1086).

Kennedy, J.F., 1963. The mechanics of dunes and antidunes in erodible-bed channels. J. Fluid Mech. 16, 521–544. doi:10.1017/S0022112063000975.

Kennedy, J.F., 1969. The formation of sediment ripples, dunes, and antidunes. Annu. Rev. Fluid Mech. 1, 147–168. doi:10.1146/annurev.fl.01.010169.001051.

Lajeunesse, E., Malverti, L., Charru, F., 2010. Bed load transport in turbulent flow at the grain scale: Experiments and modeling. J. Geophys. Res. 115, F04001.

Lang, J., Sievers, J., Loewer, M., Igel, J., Winsemann, J., 2017. 3D architecture of cyclic-step and antidune deposits in glacigenic subaqueous fan and delta settings: Integrating outcrop and ground-penetrating radar data. Sedimentary Geology 362, 83 – 100. doi:10.1016/j.sedgeo.2017.10.011.

Li, J., Qi, M., 2015. Local scour induced by upstream riverbed level lowering. Nat. Hazards 77, 1811–1827.

Lumbroso, D., Gaume, E., 2012. Reducing the uncertainty in indirect estimates of extreme flash flood discharges. Journal of Hydrology 414-415, 16–30. doi:10.1016/j.jhydrol.2011.08.048.

Maejima, W., Hota, R., Mishra, B., 2009. Antidunes and antidune stratification in the Permo-Carboniferous Talchir Formation, Talchir Gondwana basin, Orissa, India. Journal of Geosciences, Osaka City University 52, 11–20.

McLean, S., 1990. The stability of ripples and dunes. Earth-Sci. Rev. 29, 131–144.

Mendoza, A., Abad, J., Langendoen, E., Wang, D., Tassi, P., Abderrezzak, K., 2017. Effect of sediment transport boundary conditions on the numerical modeling of bed morphodynamics. J. Hydraul. Eng. 143, 04016099.

Meyer-Peter, E., Müller, R., 1948. Formulas for bed load transport, in: IAHR (Ed.), 2nd meeting, Stockholm, Sweden. pp. 39–64.

Monnier, J., Couderc, F., Dartus, D., Larnier, K., Madec, R., Vila, J.P., 2016. Inverse algorithms for 2D shallow water equations in presence of wet dry fronts: Application to flood plain dynamics. Advances in Water Resources 97, 11–24. doi:10.1016/j.advwatres.2016.07.005.

Nabi, M., Giri, S., Iwasaki, T., Kimura, I., Shimizu, Y., 2014. Multi-scale modelling of river morphodynamics, pp. 1253–1259.

Nakagawa, H., Tsujimoto, T., 1980. Sand-bed instability due to bed load motion. Journal of the Hydraulics Division, ASCE 106, 2029–2051.

Nakagawa, H., Tsujimoto, T., 1984. Spectral analysis of sand bed instability. J. Hydraul. Eng. 110, 467–483. doi:10.1061/(ASCE)0733-9429(1984)110:4(467).

Nelson, J., Shimizu, Y., Abe, T., Asahi, K., Gamou, M., Inoue, T., Iwasaki, T., Kakinuma, T., Kawamura, S., Kimura, I., Kyuka, T., McDonald, R., Nabi, M., Nakatsugawa, M., Simões, F., Takebayashi, H., Watanabe, Y., 2016. The international river interface cooperative: Public domain flow and morphodynamics software for education and applications. Adv. Water Resour. 93, 62–74. doi:10.1016/j.advwatres.2015.09.017.

Nezu, I., Nakagawa, H., 1993. Turbulence in open-channel flows. CRC Press.

Niemann, S., Fredsøe, J., Jacobsen, N., 2010. Sand dunes in steady flow at low froude numbers: Dune height evolution and flow resistance. J. Hydraul. Eng. 137, 5–14.

Núñez-González, F., Martín-Vide, J., 2011. Analysis of antidune migration direction. J. Geophys. Res. Earth Surf. 116, F02004. doi:10.1029/2010JF001761.

Olsen, N., 2017. Numerical modelling of downstream migrating antidunes. Earth Surf. Proc. Land. 42, 2393–2401. doi:10.1002/esp.4193.

Pardee, J., 1942. Unusual currents in Glacial Lake Missoula, Montana. GSA Bulletin 53, 1569–1599. doi:10.1130/GSAB-53-1569.

Parker, G., 1975. Sediment inertia as cause of river antidunes. ASCE J. Hydraul. Div. 101, 211–221.

Parker, G., Toro-Escobar, C., Ramey, M., Beck, S., 2003. Effect of floodwater extraction on mountain stream morphology. J. Hydraul. Eng. 129, 885–895. doi:10.1061/(ASCE)0733-9429(2003)129:11(885).

Periáñez, R., Abril, J., 2015. Computational fluid dynamics simulations of the Zanclean catastrophic flood of the Mediterranean (5.33Ma). Palaeogeography, Palaeoclimatology, Palaeoecology 424, 49–60. doi:10.1016/j.palaeo.2015.02.017.

Recking, A., Bacchi, V., Naaim, M., Frey, P., 2009. Antidunes on steep slopes. J. Geophys. Res. Earth Surf. 114, F04025. doi:10.1029/2008JF001216.

Reynolds, A.J., 1965. Waves on the erodible bed of an open channel. J. Fluid Mech. 22, 113–133. doi:10.1017/S0022112065000630.

Richards, K.J., 1980. The formation of ripples and dunes on an erodible bed. J. Fluid Mech. 99, 597–618. doi:10.1017/S002211208000078X.

Rudoy, A.N., 2002. Glacier-dammed lakes and geological work of glacial superfloods in the late Pleistocene, southern Siberia, Altai mountains. Quaternary International 87, 119–140. doi:10.1016/S1040-6182(01)00066-0.

Schmid, P.J., Henningson, D.S., 2001. Stability and Transition in Shear Flows. Springer.

Seminara, G., 2010. Fluvial sedimentary patterns. Annu. Rev. Fluid Mech. 42, 43–66. doi:10.1146/annurev-fluid-121108-145612.

Shaw, J., Kellerhals, R., 1977. Paleohydraulic interpretation of antidune bedforms with applications to antidunes in gravel. Journal of Sedimentary Re-

search 47, 257–266. doi:10.1306/212F7149-2B24-11D7-8648000102C1865D.

Shuwei, Z., Heqin, C., Shuaihu, W., Shengyu, S., Wei, X., Quanping, Z., Yuehua, J., 2017. Morphology and mechanism of the very large dunes in the tidal reach of the Yangtze River, China. Continental Shelf Research 139, 54–61. doi:10.1016/j.csr.2016.10.006.

Vellinga, A., Cartigny, M., Eggenhuisen, J., Hansen, E., 2018. Morphodynamics and depositional signature of low-aggradation cyclic steps: New insights from a depth-resolved numerical model. Sedimentology 65, 540–560. doi:10.1111/sed.12391.

Vesipa, R., Camporeale, C., Ridolfi, L., 2012. A shallow-water theory of river bedforms supercritical conditions. Phys. Fluids 24, 094104. doi:10.1063/1.4753943.

Wilkerson, G., Parker, G., 2011. Physical basis for quasi-universal relationships describing bankfull hydraulic geometry of sand-bed rivers. J. Hydraul. Eng. 137, 739–753. doi:10.1061/(ASCE)HY.1943-7900.0000352.

Winsemann, J., Alho, P., Laamanen, L., Goseberg, N., Lang, J., Klostermann, J., 2016. Flow dynamics, sedimentation and erosion of glacial lake outburst floods along the Middle Pleistocene Scandinavian Ice Sheet (northern central Europe). Boreas 45, 260–283. doi:10.1111/bor.12146.

Winsemann, J., Brandes, C., Polom, U., 2011. Response of a proglacial delta to rapid high-amplitude lake-level change: an integration of outcrop data and high-resolution shear wave seismics. Basin Research 23, 22–52. doi:10.1111/j.1365-2117.2010.00465.x.

Wu, G., Yang, Z., Zhang, K., Dong, P., Lin, Y.T., 2018. A non-equilibrium sediment transport model for dam break flow over moveable bed based on non-uniform rectangular mesh. Water 10. doi:10.3390/w10050616.

Wu, W., 2007. Computational River Dynamics. Taylor & Francis, London.

Zhang, S., Duan, J.G., Strelkoff, M., 2013. Grain-scale nonequilibrium sediment-transport model for unsteady flow. J. Hydraul. Eng. 139, 22—-36.